Forced Oscillators with Dynamic Hopf Bifurcations and applications to Paleoclimate.

A DISSERTATION
SUBMITTED TO THE FACULTY OF THE GRADUATE SCHOOL
OF THE UNIVERSITY OF MINNESOTA
BY

Samantha Megan Oestreicher

IN PARTIAL FULFILLMENT OF THE REQUIREMENTS
FOR THE DEGREE OF
Doctor of Philosophy

Richard McGehee

May, 2014

Acknowledgements

There are many people that have earned my gratitude for their contribution to my time in graduate school.

I would like to thank my advisor, Dick McGehee for his encouragement and insights throughout the years. To the Mathematics and Climate Research Network for providing me with a vast number of opportunities to collaborate, present, and research with other climate researchers across the US and abroad. In particular, a heartfelt thank you to Mary Lou Zeeman for her encouragement and for being a brilliant role model to me and other women in mathematics. I would also like to thank Rick Moeckel, Max Jodeit, Chris Jones, Clarence Lehman, Pam Martin, and Kathy Klink. I am continually thankful for Christopher Golé whose mentorship, teaching, and excellent conversation have inspired me for all the years since I left his classroom.

Support comes in many forms, and I would especially like to thank my family, past and present, for their support and feedback through my process. And thank you to all the friends who have supported my travel, stress and successes. A special thanks to Alanna Hoyer-Leitzel, Bryan Poling, Julie Leifeld, Jenn Koonz, Tess Kornfield, Christy Willoughby and Jason Schumacher for being true friends to me. I would not have made it through graduate school without the love and encouragement I received from these people.

Abstract

Mathematical modeling is an important tool for understanding historic and future climate. The 100,000 year problem, or the mid-Pleistocene transition, has generated a variety of models to understand Earth's climate. In this work a collection of dynamic Hopf bifurcation models are analyzed to isolate the problems and challenges of this type of model. A classic Maasch and Saltzman model is shown to be insufficient. Hopf bifurcation is generalized to the McGehee and Peckham model to conclude that, in certain idealized situations, the phase of a numerical solution can be predicted. However, when small stochastic noise is added to the system, all structure is lost. Dynamic Hopf bifurcation models do not reproduce the phase correlations which δ^{18}O has with obliquity and eccentricity. Some directions for future mathematical research are described and several oddities about quasi-periodic forcing of a Hopf bifurcation model are presented. Finally a discussion of discontinuing the use of dynamic Hopf bifurcations in mid-Pleistocene transition research is presented. Dynamic Hopf bifurcations provide a rich field for mathematical inquiry. However, as the understanding of the δ^{18}O data and of dynamic Hopf bifurcations increases, the Hopf bifurcation models become less viable choices for modeling the mid-Pleistocene transition.

Contents

List of Tables

List of Figures

Chapter 1

Introduction

- Chapter 1 introduces the analytic goals pursued in this thesis.
- Chapter 2 briefly presents the history of, and science behind, mid-Pliestocene transition dynamic Hopf Bifurcation Models.
- Chapter 3 describes the Maasch and Saltzman model of 1990 and its deficiencies.
- Chapter 4 presents a new version of the Maasch and Saltzman model which incorporates external forcing in a more realistic way.
- Chapter 5 describes the generalized Hopf bifurcation map of McGehee and Peckham and presents general results and conjectures on predicting phase angle of a trajectory post-Hopf bifurcation.
- Chapter 6 expands on the McGehee and Peckham model by offering analysis on stochastic noise as well as presenting a finer version of the model and its phase analysis.
- Chapter 7 discusses of application general theory to climate models and Earth.
- Chapter 8 provides conclusion to this thesis.

Chapter 2

History of mid-Pleistocene Transition Models

2.1 Science of the mid-Pleistocene Transition

Scientists studying climate change have a unique challenge because humans are living in our only Petri dish. Scientists cannot test a hypothesis without living through the consequences. With our Petri dish's atmospheric carbon levels climbing, understanding the short and long term cycles of our climate is crucial. In this work, we will restrict our focus to the long term cycles. An important step in understanding the long term cycles is to isolate and model the key climate driving forces. Once scientists identify the important global forces, they may more accurately predict how the recent carbon spike will affect the planet in the long run. This section is a review of current state of climate data gathering, analysis and modeling.

Mathematical modeling is an important tool for understanding the climate. Mathematicians have long been involved with understanding the climate. From Adhemar's first estimation of the orbital variations in 1842, mathematicians have tried to build transparent models to understand glacial cycles [1]. Previous work in the subject suggests the most important variables in the last million years are atmospheric temperature, atmospheric carbon, and ice boundary location [2, 3, 4]. Several contemporary minimal complexity climate models will be reviewed including Budyko-Sellers-Widiasih and Saltzman-Maasch.

Earth's temperature can be measured in paleotime by the proxy, δ^{18}O. As there are many published explanations for the relationship between δ^{18}O and Earth's average temperature, we refer the reader to the articles of Hays et al. (1976) and Petit et al. (1999) for further details on that relationship [5, 6]. For the purposes of this thesis, we take the δ^{18}O to be some function which is mostly due to planetary ice mass and partly due to temperature. Figure 2.1 shows the δ^{18}O for the last 4.5 million years which was created from ice core and sediment data.

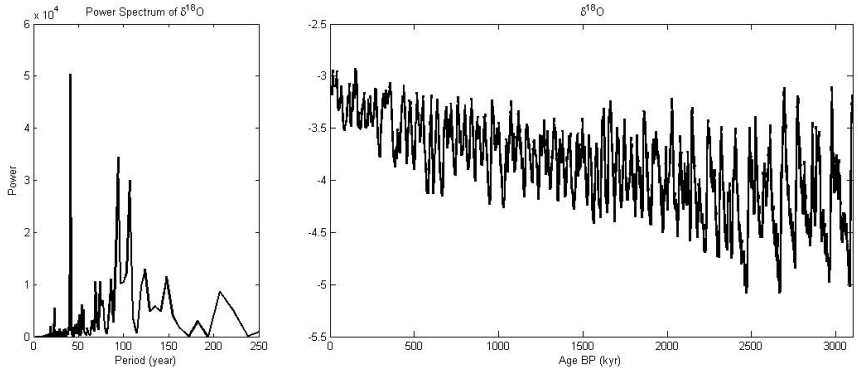

Figure 2.1: This is the last 4.5 million years of δ^{18}O data which can be thought of as a proxy for a combination of global temperature and ice mass. Data is from Lisiecki and Raymo (2005) [7].

Earth's climate has been varying between glacial and interglacial cycles throughout the Pliocene (5.3 to 2.5 million years ago) and Pleistocene (2.5 million years ago to present) [6, 8]. Classic Milankovitch theory hypothesizes that these variations are the effect of the Earth's celestial movements through our solar system [9, 10, 11, 12].

There are three main celestial movements that affect the amount of incoming solar radiation, or insolation, Earth receives: eccentricity, obliquity, and precession. **Eccentricity** is the measure of how round the elliptic orbit around the sun is. The eccentricity of this ellipse affects the climate of the Earth on a time scale of 100 kyr. **Obliquity** is a measurement of the tilt of the Earth. We measure this tilt relative to the line which is perpendicular to the plane of the ecliptic. Obliquity oscillates between 22.1^o and 24.5^o on a scale of 41 kyr. **Precession** is the circular rotation of the Earth's axis of rotation around 'straight up'. The cycle of change happens on a faster time scale of 23 kyr.

Several features can been identified from the data used to produce Figure 2.1. The

dominant period throughout the Pliocene is 41 kyr and thought to be associated with obliquity [13, 14]. However, 1.2 million years ago (myr) during the mid-Pleistocene the dominant periodicity altered to a 100 kyr cycle. An air of mystery surrounds what is known as the **mid-Pleistocene transition** (MPT) because although the new period matches that of eccentricity, the power of the eccentricity signal is much smaller than that of obliquity and is decreasing [15, 12, 16, 17]. Continued power of obliquity conjoined with the decreasing power of eccentricity suggest that the Earth system did not just move from responding from one forcing to another; there must be another explanation. These facts suggest that Earth's climate is nonlinearly affected by the Milankovitch cycles and/or affected by other features of the Earth system. Knowing precisely why the 100kyr cycle appears so strongly in the $\delta^{18}O$ data is still an open question in Paleoclimatology and will be discussed in further detail here.

The Earth's glacial cycles are affected by elements of the Earth system as well as the previously discussed Milankovitch cycles. An important component of the Earth system that can affect the glacial cycles is atmospheric carbon. Due to the properties of atmospheric carbon as a greenhouse gas, the carbon dioxide levels of the atmosphere are also of great interest to this research [4, 18]. The Mauna Loa Observatory has been faithfully collecting consistent atmospheric data which can be understood as a global average of CO_2 [19, 20]. The compilation of all the recent carbon data collected is shown in Figure 2.2.

The two most obvious features of this graph are the local oscillations and the long-term upward curve. The small oscillations are from the yearly growth and decay of terrestrial flora [21]. This is a result of northern hemisphere biomass growth and is fairly well understood. However, the yearly average CO_2 levels create a concave up curve that is rapidly increasing. This non-linear increase of CO_2 levels is cause for concern among scientists. Data from Mauna Loa Observatory shows that atmospheric carbon levels are above 380 ppm. Scientists have reconstructed carbon dioxide data records from sediment and ice cores that cover the last 55 million years. The global historical norm is 180-280ppm for the last 400 kyr [6, 22].[1] Earth has certainly moved outside the recent historical range.

[1] Though, for times before 35 million years ago, the atmospheric CO_2 values were well above 1000 ppm, but for the purposes of this research, these ancient climates are irrelevant and will not be discussed further.

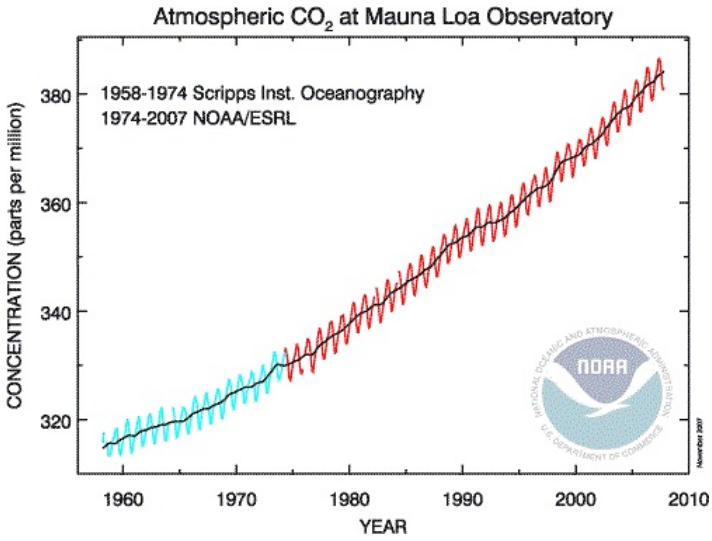

Figure 2.2: The Mauna Loa Observatory Data is also know as the Keeling Curve. Data from earlier years are from measurements done by NOAA, but in the 1970's Scripps began taking measurements at the Mauna Loa Observatory. The data is considered to be uninterrupted and a precise account of the global state of the atmosphere over the last 50 years.

2.2 Minimal Complexity modeling before 1976: Budyko-Sellers

In the late 1960's Budyko and Sellers separately but simultaneously produced similar global energy balance models of Earth. The Budyko-Sellers model initially only included insolation and ice albedo feedback [23, 24]. The model was streamlined by North and is given in Equation 2.1 [25]. The model gives the annual mean temperature, T, at each latitude.

$$R\frac{dT(y)}{dt} = (1 - \alpha(T(y))) \cdot Q \cdot s(y) - (A + BT(y)) + C(\overline{T} - T(y)) \tag{2.1}$$

This is a basic energy balance equation: change in energy, $\frac{dT}{dt}$, is proportional to energy in - energy out. The additional third term, $C(\overline{T} - T(y))$, is an energy transfer term between each latitudinal band which will be discussed further below.

In Equation 2.1, the free variable is $y = \sin(\theta)$ where θ represents latitude on the planet. Earth is assumed to be symmetric about its equator. Thus $\theta \in [0, \pi]$ which implies $y \in [0, 1]$. Annual mean temperature, T, is as a function of latitude, $T(y)$. The other variables are as follows: R is the heat capacity of the planet's surface as dictated by the land and ocean. Q is the annual average insolation, representing how much energy is received by the outer edge of the atmosphere from the sun. Then, because of the axial tilt and other confounding factors, $s(y)$ is needed to give the latitudinal distribution of that energy. As such, $s(y)$ is defined such that $\int_0^1 s(y)dy = 1$. ($|s|_{L^1} = 1$) We will use the definition $s(y) = \frac{1-0.481(3y^2-1)}{2}$, as in an approximation by North [25]. The annual average surface temperature at latitude $\arcsin(y)$ is $T(y)$. Thus $T(y)$ is a temperature profile over the unit interval. The α function, $\alpha(T(y))$, represents surface albedo which is based on the temperature at each latitude. North defines α as the piecewise constant function:

$$\alpha(T(y)) = \begin{cases} \alpha_1 = 0.38 & \text{for } T > T_c \\ \alpha_2 = 0.68 & \text{for } T < T_c \end{cases}$$

The critical temperature, T_c, is the temperature required to form glaciers. Glacier ice reflects more insolation than open water, so the albedo is higher for colder temperatures. We use the definition of $T_c = -10^oC$, the average temperature to freeze sea-ice. This function is constructed under the assumption that each latitude is either ice-free or ice-covered. There is no transition zone. Thus, the $(1 - \alpha)$ term in Equation 2.1 describes the percentage of insolation that is absorbed by the planet at a given latitude.

$A + BT$ represents the energy lost due to black body radiation. Typical values are $A = 202\ W/m^2$, $B = 1.9\ W/m^2C$ [26]. The radiation term is based on observational outgoing long wave radiation and has been linearized for ease of computation. Lastly, $C(\overline{T} - T)$ models the heat transport where $\overline{T}$ is the average surface temperature. The assumption is that energy transport will not change the overall energy stored on the planet, but the energy at each latitude will relax towards the mean. Thus, transport is assumed to be a linear relaxation of energy as the temperature tries to equalize and homogenize. We define $C = 3.04\ W/m^2C$ [26].

The beauty of this model is its simplicity. However, there are some limitations: the location of the ice line at equilibrium can be unrealistic. The model can find an

equilibrium solution, but it is not equipped to simulate a dynamic, or moving, ice line. From a wide range of initial conditions this model behaves in a very non-realistic way [27]. To more accurately simulate reality, Esther Widiasih added an equation to alter the motion of the ice line. Her updated Budyko-Sellers-Widiasih model is:

$$\begin{aligned} T_{t+1} - T_t &= \frac{1}{R}((1-\alpha(y,\eta))Qs(y) - (A+BT(y)) + C(\overline{T} - T(y)) \\ \eta_{t+1} - \eta_t &= k\epsilon(T(\eta) - T_c) \end{aligned} \tag{2.2}$$

With all the variables defined as above except α:

$$\alpha(T(y)) = \begin{cases} \alpha_1 = 0.38 & \text{for } T > T_c \\ \alpha_0 = \frac{\alpha_1+\alpha_2}{2} = 0.53 & \text{for } T = T_c \\ \alpha_2 = 0.68 & \text{for } T < T_c \end{cases}$$

This model is organized as a difference equation because there is a smallest time step at which it makes sense to consider the system. Any time step smaller than 1 year has no physical meaning as T is defined to be the annual average temperature. Notably, this model has the result that with α as a function of η, there are only two equilibrium solutions to the system in Equation 2.2 [3].

Later, McGehee and Widiasih returned to the problem and began treating Equation 2.2 as though it were a differential equation as in Equation 2.1 [28]. McGehee and Widiasih then completed a Legendre polynomial expansion of Equation 2.2 and together with a change of variables simplified the system to a one dimensional differential equation which approximates the movement of the ice line on an exponentially attracting invariant curve [28]. The new formulation of the equations on the system's center manifold is as follows:

$$\begin{aligned} \dot{\eta} &= \epsilon h(\eta) \\ h(\eta) &= \left(\Phi_0(\eta) + \frac{Qs_2(1-\alpha_0)}{B+C}p_2(\eta) - T_c\right) \\ \Phi_0(\eta) &= \frac{1}{B}\left(Q(1-\alpha_0) - A + C\frac{Q(\alpha_2-\alpha_1)}{B+C}\left(\eta - \frac{1}{2} + s_2 P_2(\eta)\right)\right) \end{aligned} \tag{2.3}$$

Where $s_2(\beta) = \frac{5}{16}\left(-2 + 3\sin^2\beta\right)$, $p_2(y) = \frac{1}{2}(3y^2-1)$ the second even Legendre polynomial, and $P_2 = \int_0^\eta p_2(y)dy = \frac{1}{2}(\eta^3 - \eta)$. Notably, for parameter values of the current climate, the equilibrium solutions of h ($h(\eta) = 0$) are $\eta_1 \approx 0.25$ and $\eta_2 \approx 0.95$

where η_2 is the stable fixed point [28]. This is a physically meaningful result and suggests that the small ice caps we currently witness on Earth are stable.

The $\dot{\eta}$ equation is particularly notable because this is a one dimensional differential equation that incorporates obliquity and eccentricity into an ice-albedo feedback model to produce meaningful ice line movement. The model uses clearly defined and physically meaningful parameters $\{A,\ B,\ C,\ \alpha_1,\ \alpha_2,\ \eta,\ T_c\}$ and several orbitally defined constants $\{Q,\ s_2\}$. In Chapter 4, we will consider how some of these parameters might change over paleotime.

However, there has always been a limitation to this classic model, it was crafted to match the prominent features of primitive observational data. No one could truly model the MPT until good paleodata were available. The first set of combined δ^{18}O data was released with Hays et al.'s 1976 paper [5]. Since then, data and age models of these data have continually improved. While data-set creation is rich and fundamental to modeling advances, data creation is outside the scope of this dissertation and so the details of these advances will not be covered here. The reader may refer to Petit (1999), Huybers (2007), and Lisiecki (2010) for further information on age models [6, 10, 13]. For the purposes of this dissertation we will treat an age model and related stack of δ^{18}O data as fact.

2.3 Post 1976: Dynamic Hopf Bifurcation Models

Several models have been developed to address the mid-Pleistocene transition post-1976 [14, 29, 30, 31]. Models developed by Korobeinikov (2010) and Maasch and Saltzman (1990) replicate the MPT by transitioning from a 41 kyr to a 100 kyr cycle through the use of a bifurcation parameter [30, 31]. The model presented by Maasch and Saltzman (1990) is a physically motivated model of the climate system in three variables: global ice mass, atmospheric CO_2, and North Atlantic deep water formation [32]. This model, which we will refer to as MS90, has internal feedbacks that produce 100kyr cycles with and without the presence of external forcing. In their 1990 paper, Maasch and Saltzman use Fourier analysis to observe that the power spectrum changes as the model goes through the observed bifurcation and matches the $\delta^{18}O$ data [31]. Additionally, they claim that the signal is locked by the Milankovitch forcing. Barry Saltzman and

co-authors wrote a collection of papers developing a model for Pleistocene climate in the late 1980s and early 1990s [31, 32, 33, 34]. Maasch and Saltzman (1990) present a model for the late Pleistocene ice ages in terms of nondimensional variables for global ice mass (X), atmospheric CO_2 (Y), and North Atlantic deep water formation (Z); the model is formulated as follows:

$$\begin{aligned} \dot{X} &= -X - Y - uM(t) \\ \dot{Y} &= -pZ + rY + sZ^2 - Z^2Y \\ \dot{Z} &= -q(X + Z). \end{aligned} \tag{2.4}$$

where $M(t)$ = Milankovitch Forcing (65^oN normalized to 0 mean and unit variance). The variables are dimensionless deviations from an equilibrium corresponding to fixed values of external forcing. For $u = 0$, there is a Hopf bifurcation in the p and r parameters that generates the major features of the MPT. The details of this model will be presented in Chapter 3.

Mathematically, a bifurcation is understood for a fixed bifurcation parameter. The mathematical complications associated with changing the bifurcation parameter with time are newly studied [29, 35]. The most common effect of a dynamic bifurcation is a delay of oscillation [36]. This dissertation attempts to shed further light on the topic of dynamic bifurcations by investigating the phase of various solution trajectories post-bifurcation.

2.4 Historically how a model is forced

Each minimal complexity model must be forced with some version of Milankovitch cycles. Much of the research has applied 65^o N summer solstice insolation. This choice is made because the mid-summer melt of glaciers is thought to be the main component that affects glacial advance and retreat [37]. This is a choice based on previous correlations that may not suit a model is averaged over a year or more. McGehee and Lehman (2012) show that precession, a major contributor to the 65^oN signal, has no effect on the average global temperature over the course of a year [16]. By forcing a model with this signal, precession effects are introduced where none should be present. In particular, Maasch and Saltzman (1990) use 65^oN to force a model which is averaged over $10,000$

years [31]. Based on celestial mechanics computations, we should not expect to see a precession signal in the model output. The model presented in this work is forced by eccentricity and obliquity values as computed by Berger (1991) [11].

The classic energy balance model produced by Budyko (1968) and Sellers (1968), along with the recent additions of Widiasih (2010) and McGehee and Widiasih (2013), elegantly uses the obliquity and eccentricity signals to solve for the equilibrium ice line solution for a simplified version of Earth [3, 23, 24, 28]. In Chapter 4, we conjoin this model with the model produced by Maasch and Saltzman (1990) to update the Saltzman model to include celestially derived orbital effects. By using the Budyko-Sellers-Widiasih model as a basis for the ice line movement, our model more accurately accounts for ice movement caused by orbital variation in a classically accepted way. Additionally, the carbon and oceanic overturning feedback from the Saltzman model is a classic formulation for these feedbacks. By coupling the two, we formulate a more complete, cohesive interaction between orbital forcing and the internal Earth climate system.

2.5 Recent advances in data analysis

In the last decade, data analysis has been integrated into the study of climate data to give new insights into paleoclimate. Three types of data analysis are: wavelet analysis, Fourier power series, and phase angle analysis [2, 5, 13, 14, 29]. These recent publications show various phase correlations between δ^{18}O and orbital forcing. While scientific consensus has not been reached, it is clear that there is a phase relationship between the δ^{18}O data and the Milankovitch cycles. In this text we will restrict our attention to the most widely accepted results of the phase angle analysis completed by Huybers and Lisiecki [13, 14]. Huybers showed that the δ^{18}O data is consistently in phase with obliquity for the last 2 myr. Lisiecki showed Earth's δ^{18}O data is phase correlated to eccentricity over the last 1.2 myr. Thus, we are going to be looking for a model that is in phase with obliquity and, once the 100 kyr cycles begin, is also in phase with eccentricity. More details on this type of analysis will be presented in Chapter 3.2 and beyond.

2.6 Thesis Statement

By considering several specific and one generalized dynamic Hopf bifurcation models, I will show that while the post-bifurcation phase of a solution can be predicted in a deterministic, minimal complexity, dynamic Hopf bifurcation model, a predictable relationship between phase and external forcing is unlikely to exist in more realistic models. Over the next five Chapters, I will present model development, model simulations, data analysis, mathematical arguments, and several conjectures in support of this statement.

Chapter 3

Classic Hopf Bifurcation Model: Saltzman

3.1 Saltzman Models

Since Barry Saltzman and his co-authors published in the late 1980s and early 1990s, scientists have discovered much more about Earth's paleoclimate [31, 32, 33, 34]. Moving past the basics of including Milankovitch cycles, authors including Lisiecki (2010) and Huybers (2007) have shown various phase locking relationships between the $\delta^{18}O$ data and the Milankovtich cycles [13, 14]. In order for a model to be accepted today it must reproduce these relationships. To this regard, a model must pace obliquity from 2 myr ago to present and must pace eccentricity from 1.2 myr ago to present.[1] In this section a classic formulation of one of Saltzman's models will be considered and the pros and cons of this classic Hopf bifurcation model will be discussed.

The chapter begins by describing the Maasch and Saltzman model from its component parts and the parameter shifts that cause the model to bifurcate from small, quick glacial cycles in the early Pleistocene to large, slower glacial cycles in the late Pleistocene [31]. The original authors have already shown that the model reasonably reproduces the time series and Fourier series of $\delta^{18}O$ and atmospheric CO_2 [31]. In

[1] Further research by these authors and others suggests there may a phase relationship between precession as well. But that is outside the realm of this study because these models are using a greater than one year time step and, over a year, precession has no effect [16].

this section, the model's ice line output will be shown to be paced by obliquity from 2 myr ago to present. The model does not appear to be paced by eccentricity. This is a result that matches Huyber's analysis of the δ^{18}O data but which does not match the data analyses by Lisiecki [13, 14]. A discussion of how this discrepancy is created follows. The chapter concludes with the claim that the Maasch and Saltzman model, as is, cannot continue to be an accepted model for the mid-Pleistocene transition.

3.2 Model Formulation and Classic Analysis of MS90

Maasch and Saltzman (1990) present a model, MS90, for the late Pleistocene ice ages in terms of nondimensional variables for global ice mass (X), atmospheric CO_2 (Y), and North Atlantic deep water formation (Z); the model, also presented in Chapter 2, is formulated as follows:

$$\begin{aligned} \dot{X} &= -X - Y - uM(t) \\ \dot{Y} &= -pZ + rY + sZ^2 - Z^2Y \\ \dot{Z} &= -q(X + Z). \end{aligned} \tag{3.1}$$

A bifurcation in the p and r parameters generates the major features of the MPT [31]. The variables are dimensionless deviations from an equilibrium corresponding to fixed values of external forcing. The parameter values are: $p = 0.8 \rightarrow 1$, $q = 1.2$, $r = 0.7 \rightarrow 0.8$, $s = 0.8$, and $u = 0.7$ where p and r vary linearly in time. Note, these slow parameter changes lead to the bifurcation and were chosen in part so that the bifurcation occurs 1.2 million years ago. The intrinsic 100 kyr oscillation in the model is driven by instability in the equation representing the atmospheric carbon cycle. Because the system is minimally complex, one can explicitly solve for eigenvalues and bifurcation locations of the unforced, $u = 0$, system. This analysis is presented by Maasch and Saltzman [31].

While understanding the unforced equation analytically is valuable, understanding how the model behaves in the presence of external forcing is also necessary. Now consider the results of forcing the system with 65 ^{o}N summer solstice insolation as defined by Berger (1991), call it Q_I [11]. To apply the forcing at the appropriate magnitude it is normalized by $M(t) = [Q_I - \text{mean}(Q_I)]/\text{std}(Q_I)$ and use $u = 0.7$ as Maasch and

Saltzman (1990) did. The author of this dissertation reproduced the same time series as Maasch and Saltzman did in the forced and unforced case. The numerical integrations of the forced model in Figure 3.1 show the bifurcation happening 1.2 million years ago, as desired. This model run and parameter choice, at first glance, captures the dominant features of the data well. As shown in Maasch and Saltzman (1990), the last 1.2 million years of the run has power at 104 kyr (not shown). This is in line with the δ^{18}O data. However, the oldest 0.8 million years of the run has power in the Fourier analysis at 21 kyr. This is the same frequency as precession. The δ^{18}O data shows a period of 41 kyr pre-MPT. Thus, even with basic analysis, MS90 does not reproduce all of the features of the δ^{18}O data.

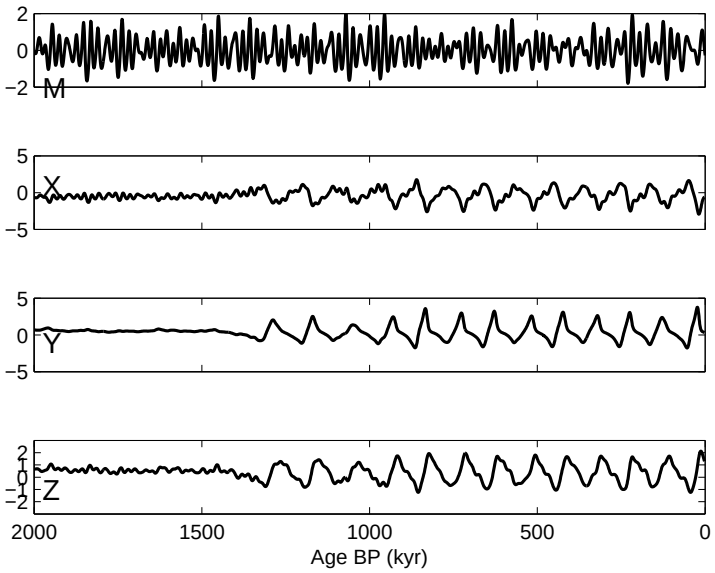

Figure 3.1: Numerical integration of model from Maasch and Saltzman, MS90 [31]. This is a representative plot using linear parameter shift $p = 0.8 \rightarrow 1,\ q = 1.2,\ r = 0.7 \rightarrow 0.8,\ s = 0.8,\ u = 0.7$ with normalized 65^oN summer solstice insolation as external forcing on the system.

3.3 Phase Analysis Results

Before the model can be shown to pace a particular external forcing, the model must not possess any intrinsic phase preferences. This means that for a given moment in time the oscillating system can be at any phase within an oscillation. For example, two different initial conditions might have two distinct trajectories which are at a different phase at the same moment in time. For fixed parameters, MS90 is a mathematically autonomous model which means, by definition, it will never have an intrinsic phase preference. Therefore, any phase correlation that is found can be attributed to the external forcing on the system and not from intrinsic model preference.

To quantify the phase difference between eccentricity or obliquity and the model results Rayleigh R circular statistics are employed. The phase analysis is modeled on the technique Huybers (2007) used [10]. The lowest moment of the forcing signal is defined to have phase 0. The moments of zero phase in the model output are defined to be deglaciations in the ice volume, X. If consecutive peak/valley pairs of X have a difference that is larger than one standard deviation of the entire model output, the midpoint in time is identified as a moment of deglaciation. Any other moment in time can be compared by linearly interpolating with respect to time between the zero-phase locations. In this way the phase of the forcing is directly compared to the phase of the model to determine the phase difference between the two time series.

Because the expected phase difference between forcing and output cannot be guessed a priori, the early portion of the data is tested with no guess as to a mean angle. The initial test is to determine if the phase difference is uniformly distributed with 99% confidence or not [38, 39]. Both early time series show angle cohesion and are not uniform (See Table 3.1). For late and full time durations, the following hypothesis is tested: H_0 is that the angles are uniformly distributed in phase. H_A is that the angles are not uniformly distributed in phase, but have a mean equal to the mean of the early time duration's phase differences. Table 3.1 shows the results of all tests. Notice, the phase differences between the model deglaciations and the obliquity forcing always show phase angle cohesion to 95% confidence or more. In contrast, the phase differences between the model deglaciations and the eccentricity forcing are related in the older years, but after the bifurcation the phase differences are uniformly distributed.

This suggests MS90 is not paced by eccentricity during the late Pleistocene.

Period	R	P	Testing H_0	Angle Error	confidence level	deglac.
Early Obl	0.711	0.023	not uniform	± 1.00	95%	8
Late Obl	0.555	0.021	RejectH_0	± 1.17	95%	12
All Obl	0.590	0.001	RejectH_0	± 0.73	95%	19
Early Ecc	0.572	0.098	not uniform	± 1.39	90%	8
Late Ecc	0.128	0.827	Can$'$t rejectH_0	$--$	$--$	12
All Ecc	0.190	0.529	Can$'$t rejectH_0	$--$	$--$	19

Table 3.1: Results of phase stability tests. All tests were run in radians with parameter values: $p : 0.8 \to 1$, $r : 0.7 \to 0.8$, $q = 1.2$, $s = 0.8$, $u = 0.7$, $M(t) = 65^o$N Insolation. The early time period is from 2 to 1.2 million years ago while the late is from 1.2 to present. $R = \sqrt{(\Sigma_i \cos\theta_i)^2 + (\Sigma_i \sin\theta_i)^2}$ where θ_i are the difference angles of each i^{th} deglaciation. P is the exceedance probability associated with obtaining a value equal or greater to R from a sample size n taken from a uniform distribution [39]. For "early" time periods, H_0 is that the angles are uniformly distributed. If H_0 is rejected at the 99% confidence level, then the angles are not uniformly distributed and the most likely average angle is found to the given confidence level. For "late" and "all" data sets, accepting or rejecting H_0 (that the angles are uniformly distributed) is always done at the 99% confidence level. If H_0 can be rejected, then H_A (The angles are not uniformly distributed in phase, but have a mean equal to the mean of the early time duration's phase difference) is accepted. The mean angle confidence intervals are listed in radians with associated confidence level [38]. For the last two eccentricity tests, H_0 can not be rejected, so no further tests are completed.

The model results of the late Pleistocene show a strong phase stability with obliquity and no phase stability with eccentricity. Figure 3.2 suggests the model is in phase with obliquity because there is a strong cohesion of the phase differences. The figure also shows the model is not in phase with eccentricity over the last 1.2 myr. More specifically, deglaciations of the model are in phase with local minima of the obliquity cycle. This is in contrast to Huybers's analysis which shows deglaciations of δ^{18}O are in phase with local maxima of the obliquity cycle. So, in this way, MS90's phase locking to obliquity is not consistent with current analysis.

Finally, despite the fact that the period of the large glacial cycle oscillations is 100 kyr, the model has very little phase response to eccentricity. This lack of phase response suggests that the intrinsic 100 kyr cycle is independent of eccentricity in this model. So, if this model is accurately modeling Earth's climate system, then the 100 kyr cycle in

Figure 3.2: Rayleigh R circular statistics of the last 1.2 million years. Obliquity phase angle is on the left, eccentricity is on the right. Radial line shows mean angle with magnitude R showing relative cohesion of angles. The inner solid circle is the magnitude R must be exceed to reject H_0. Stars along the outer circle are individual phase angle differences. A radial line pointing straight up would show the model is in phase with the local maxima of the forcing term. A radial line pointing straight down would show the model is in phase with the local minima of the forcing term.

the δ^{18}O would have no relationship to the eccentricity forcing. Thus, for our planet's climate data, the fact that the natural 100 kyr cycle of the planet has the same period as the eccentricity signal is simply a cosmic coincidence and not causal.

Mathematical artifacts of precession are present in this analysis but were not considered further because they are not a meaningful forcing on MS90. Because the model is forced in the X component and the output of the X data is being used to determine phase pacing, local features are more likely to pace the strongest signal of any period than the weaker ones. That is to say, because 65 ^{o}N insolation is dominated by 19 and 23 kyr cycles of the the precession signal, the model should, and does, show a strong phase stability with the precession signal (not shown). However, further study into precession was not undertaken because precession is not a meaningful forcing on MS90. Effects of precession cannot be considered in any global yearly average model (in particular in SM90) because, over the course of a year, precession has no effect on our planet [16]. Notably, the model still shows strong phase stability with obliquity despite 65 ^{o}N being mostly precession modulated by eccentricity.

Now it can be concluded that Maasch and Saltzman's original 1990 Hopf bifurcation model is insufficient. Initially a model must match the time series of the processes it is trying to reproduce. But because there are many models that can be crafted to reproduce the MPT, more must be shown. The above analysis has shown that the

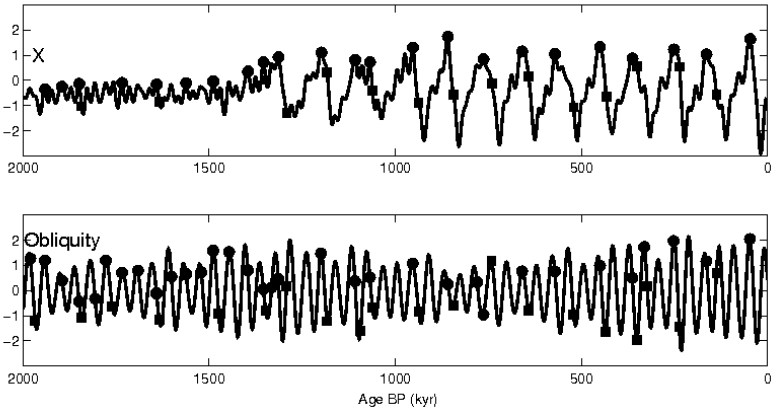

Figure 3.3: A comparison of the relative phase differences of choosing the midpoint of glacial advance (squares) to the initiation of deglactiation (circles) of the X variable (above) to obliquity forcing(below). The timing of the midpoint of deglaciation and initiation of deglaciation are projected onto the forcing to better visualize the locations of those moments in time.

model is paced by obliquity for the last 2 myr. This is a result that matches Huybers's analysis of the δ^{18}O data but which does not match the data analyses by Lisiecki [13, 14]. However, the details of Huyber's analysis are not reproduced; SM90 does not produce moments of deglaciation which happen at the same time as at peaks of obliquity. So, as is, MS90 is not a model worth pursuing because it does not reproduce the relationships found in the δ^{18}O data. There is an additional problem of how the model is forced. Because the external forcing term is a summand to the ice line equation, there is a possibility that this is too simple of a mechanism to account for all the effects of the cycles. It is possible that the formulation of the model is sound, but the application of Milankovitch forcing is too simplistic to be accurate. Thus there are several motivations for revamping Saltzman's model before using it to study the Mid-Pleistocene transition:

1. Saltzman models need to be updated because better $\delta^{18}O$ data is now available to analyse and provide a better understanding of how $\delta^{18}O$ interacts with Milankovitch cycles. The original formulations do not reproduce what is now seen in the climate data. Most grossly, the model should have a 41 kyr period before the MPT.

2. The Saltzman models do not apply external forcing in a meaningful way. In particular, precession cancels out over a year average. Since the time scale is 10^5 yrs, precession should not be included in the forcing terms. [2]

There are models that do an excellent job of ice/albedo feedback. One such model is the Budyko-Sellers-Widiasih (BSW) model which was introduced in Equation 2.2. The benefit of the BSW model is that it relies only on obliquity and eccentricity. By using the BSW model as a basis for the ice line movement, the model more accurately accounts for ice movement caused by orbital variation in a classically accepted way. However, there are many things that the MS90 model does well. The carbon and oceanic overturning feedback from MS90 is a classic model formulation for these feedbacks. Combining the models may fix the current problems with how MS90 handles Milankovitch cycles and how the model does not match eccentricity phasing in the same way the δ^{18}O does. In Chapter 4, BSW will be coupled to MS90 to formulate a more complete, cohesive interaction between orbital forcing and the internal Earth system.

[2] More generally, the author of this dissertation holds that forcing a model with insolation values for a particular day of the year at a particular latitude is a poor choice when using a model which is averaged over $1,000$ years.

Chapter 4

Improved dynamic Hopf bifurcation Model

In this Chapter, two classic models will be combined and tested to see if the combination has the strengths of both. From Maasch and Saltzman's 1990 model, the model will gain an earth, ocean, and atmosphere system with large period internal cycles. From the Budyko-Sellers-Widiasih model (BSW), the model will gain a solid connection between celestial mechanics and ice-albedo feedback. In McGehee and Widiasih (2014), the authors distill all the dynamic aspects of the BSW model to one equation that yields dynamic information about the equilibrium ice line as obliquity and eccentricity change [28]. This dynamic ice line (η) equation, here referred to as $\frac{\partial \eta}{\partial t}$, will be used as a replacement for the ice mass equation in Maasch's model. While there is a distinct difference between ice line and ice mass, the development of the Maasch and Saltzman model relies primary on the idea that large ice mass will have a greater sea ice extent in the northern pole. Thus, qualitatively, Maasch's normalized ice mass and Widiasih's ice area/line satisfy the same dynamics. By maintaining the shape of the atmospheric CO_2, μ, and North Atlantic deep water formation, ω, equations, the two models will be coupled together to formulate an energy balance model which is not affected by precession.

4.1 Model Formulation

The new model will be produced by combining the $\dot{\eta}$ equation from Widiasih and McGehee (2014) with the atmospheric CO_2 and North Atlantic deep water formation equations from Maasch and Saltzman (1990) [31, 28]. The $\dot{\eta}$ equation will incorporate all the dynamic aspects of the BSW model and will give dynamic information about the movement of the ice line. This will be coupled to the atmospheric carbon dioxide and north Atlantic deep water formation equations from MS90. The equations of the new model, called MS90BSWM (Budyko, Sellers, Widiasih, McGhee), are as follows:

$$\begin{aligned}
\dot{\eta} &= \epsilon\left(\left(\frac{CQs_2(\alpha_2-\alpha_1}{2B(B+C)}\right)\eta^3+\right. \\
&\quad \left(\frac{3Qs_1(1-\alpha_0)}{2(B+C)}\right)\eta^2+\left(\frac{CQ(\alpha_2-\alpha_1)}{B(B+C)}\right)\left(1-\frac{s_2}{2}\right)\eta+ \\
&\quad \left.\frac{2(B+C)(Q(1-\alpha_0)-A)-CQ(\alpha_2-\alpha_1)-BQs_2(1-\alpha_0)}{2B(B+C)}-T_c\right) \\
\dot{\mu} &= -p\omega+r\mu+s\omega^2-m\omega^2\mu \qquad (4.1)\\
\dot{\omega} &= -q(f(\eta)+\omega)
\end{aligned}$$

α_1	$=0.32$	p	$=0.8$	$A(\mu)$	$=-3\mu+205.5$
α_2	$=0.62$	q	$=1.8$	$C(\omega)$	$=0.05\omega+3$
α_0	$=(\alpha_1+\alpha_2)/2$	m	$=1$	$f(\eta)$	$=-16\eta+13.2$
B	$=1.9$	T_c	$=-10$	s_2	$=(5/16)(-2+3\sin\beta^2)$

Table 4.1: Constant values and translation/projection equations for MS90BSWM.

Here α_1 is the albedo on the equator side of the ice line and α_2 is the planetary albedo poleward of the ice line. The average of the two is α_0 and is the value of Earth's albedo at the ice line. Q is the yearly average insolation of the planet as a function of eccentricity, ε. $Q = \frac{343}{1-\varepsilon^2}$. Obliquity is represented by β. The values of both β and ε are defined as in Berger (1991) with a Matlab file by Ian Eisenman and Peter Huybers [11]. Note, if the model is run without an external forcing term, constant values for ε and β must be chosen. Define $\beta = 23.5$ and $\varepsilon = 0$ so that $Q = 343$. The distribution of the insolation over the latitudes as a function of obliquity is called $s_2(\beta)$.

The η equation in Equation 4.1 can be viewed as a third order polynomial in η with coefficients dependent on $\beta,\ \epsilon,\ \mu$, and ω as in Equation 4.2.

$$C_1(\beta,\epsilon,\omega)\eta^3 + C_2(\beta,\epsilon,\omega)\eta^2 + C_3(\beta,\epsilon,\omega)\eta + C_4(\beta,\epsilon,\omega,\mu) \tag{4.2}$$

The reader may note that μ is only present in C_4. Notably, the η equation obtains values on $[0,1]$ while the μ and ω equations must oscillate above and below $\mu = 0$ and $\omega = 0$ to behave appropriately. Thus, several functions are needed to translate from the deviations away from the mean in μ and ω to true values of atmospheric carbon in parts per million (ppm) as well as north Atlantic overturning circulation in Sverdrup (Sv). From the original Budyko-Sellers equation, it has been shown that A can be viewed as a function of atmospheric CO_2 (or more generally a function of atmospheric thickness via greenhouse gases, possibly). Thus, in MS90BSWM, A is a function of μ [40]. The energy relaxation constant, C, from the $C(T-\overline{T})$, is a function of the deep water formation, ω. This is because much of the energy transport from equator to pole is moved by the oceans [4][Chapter 7]. Additionally an equation that maps η from its Pleistocene range of $[0.7, 0.95]$ to $[-2, 2]$ is needed. These projections are the purpose of equations $A(\mu)$, $C(\omega)$ and $f(\eta)$ defined in Table 4.1.

Parameters $m,\ p$, and q are always held constant and are defined in Table 4.1. During the dynamic bifurcation, several parameters of the system will change with time. The dynamic variables are ϵ ($\epsilon << 1$), $\ r,\ s$ and are numerically defined with respect to a in Table 4.2. Please note, these parameters are different than the ones used in MS90. The parameter shift presented here has been adjusted for the change in the η variable. The parameter choice and shift was inspired by other work of Saltzman but is unique to this model. This parameter shift decreases the size of ϵ thereby slowing down the movement of the ice line. This is a representation of the belief that as the glacial cycles repeated, the overall area of coverage remained the same, but glaciers in later glacial cycles were significantly thicker than previous ones. The greater depth is represented by slower movement of the ice line. For physical interpretation of the changes in r and s the reader is directed to Saltzman and Maasch (1988) [32]. Because the equations were non-dimensionalized, the process of determining physical meaning is less clear.

One can numerically find the bifurcation with respect to the parameter a. The equilibrium solution is approximately $(\eta, \mu, \omega) = (0.807505, -0.981334, -0.279914)$ and for

a parameter value of $a = 0.081548252$ the eigenvalues of the system are approximately $\lambda_1 = -3.54536$ and $\lambda_{2,3} = +/-1.44067i$. Thus, there is a candidate for a Hopf bifurcation in MS90BSWM at $a \approx 0.82$ and numerical simulations indicate that the bifurcation is supercritical. Therefore, MS90BSWM is a dynamic Hopf bifurcation model in three variables. The numerical solution for MS90BSWM can be seen in Figure 4.1.

parameter	nondymanic	dynamic
$r(a)$	0.3	$\min(0.3 + 0.3a, 0.6)$
$s(a)$	0.2	$\min(0.2 + 0.3a, 0.5)$
$\epsilon(a)$	4×10^{-12}	$\max(4 \times 10^{-12} - 2a \times 10^{-12}, 2 \times 10^{-12})$
$a(t)$	0	$H[t - (t_{end}/a_1)] \min(\frac{t-(t_{end}/a_1)}{t_{end}/a_2)}, 1)$

Table 4.2: Parameter values for Equation 4.1. H is a Heaviside function, $a_1 = 3.5$, $a_2 = 2$, t is time and t_{end} is the earliest moment in time. The model ran for a simulated time of 10^5 yrs.

4.2 Phase Analysis Results

This section will cover the results of the new conjoined model.

First, the model is compared to δ^{18}O and atmospheric CO_2 data. Figure 4.2 shows the time series for ice mass lines up well with the data for δ^{18}O from Lisiecki and Raymo (2005) [41]. Figure 4.2 also shows the time series of the last 400kyr for atmospheric CO_2 from Epica. The model also correlates favourably to the major recent time series features in the data including asymmetrical oscillations.

But any model can be tuned to match the time series with enough constants. Fourier power spectrum of the whole series (see Figure 4.3) shows power predominantly at a period 98 kyr with some power at higher frequencies. Notably, the power spectrum of the first 1.8 myr of simulated time has a dominant period of 41.1 kyr while the last 1.2 myr of simulated time has a dominant period of 100.0 kyr. Thus, as can also be viewed with the naked eye, there is a clear distinction between pre-MPT and post-MPT. This is an improvement over MS90. MS90 has a period of 21 kyr pre-MPT which is not consistent with the δ^{18}O data. By having a more integrated approach to including external forcing, MS90BSWM more accurately models the period of the δ^{18}O data pre-MPT.

Finally, Rayliegh R circular statistics phase angle analysis are applied to MS90BSWM

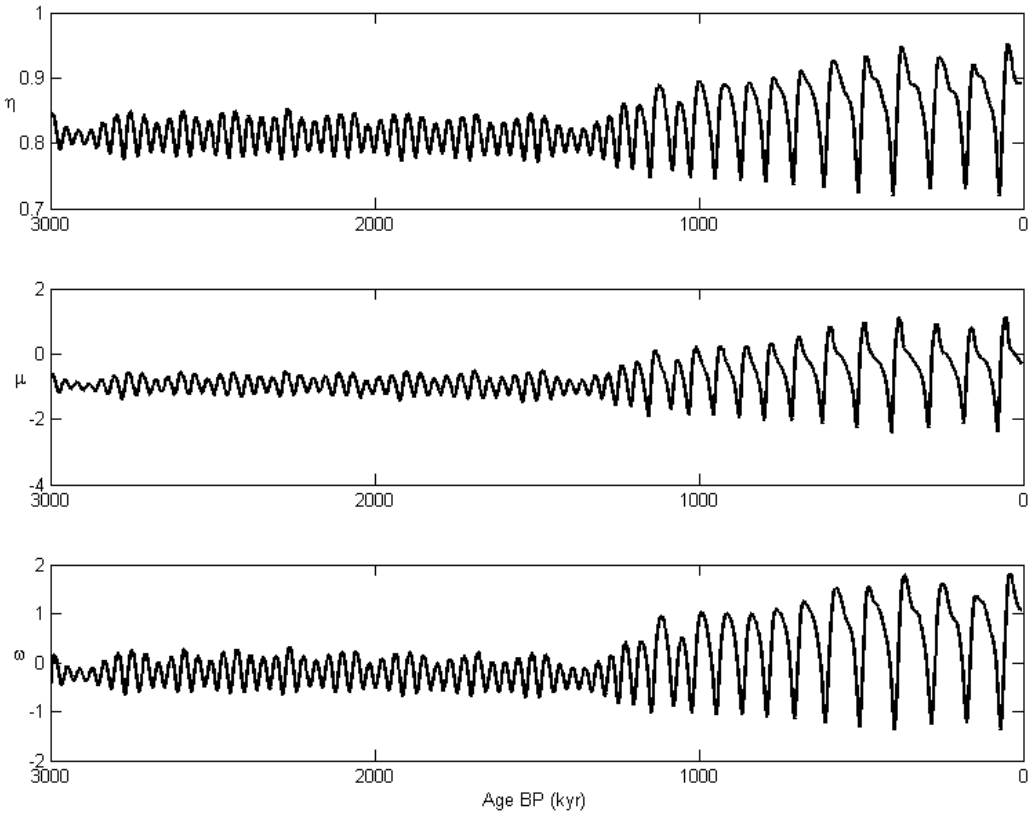

Figure 4.1: Numerical solution for MS90BSWM model using parameter shifts as defined in Table 4.2 for a simulated time of 3 myr.

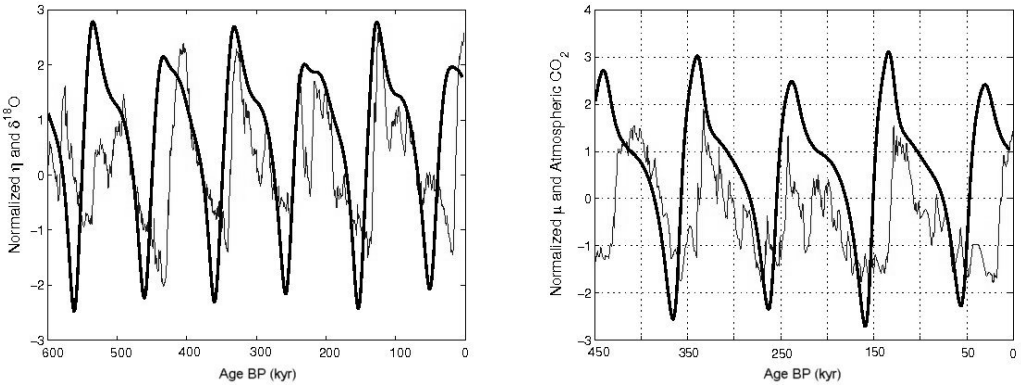

Figure 4.2: Left: Ice mass data for the last 600 kyr. The thin curve data is δ^{18}O data from the supplement to Lisiecki (2005). The thick curve is output from MS90BSWM [41]. Right: Atmospheric CO_2 comparison for the last 450 kyr. Normalized atmospheric CO_2 data from Luthi (2008) is shown as a thin curve and normalized model output of atmospheric CO_2 is shown as a thick curve [42].

à la Lisiecki (2010) and Huybers (2011) [13, 14]. See Figure 4.4. The model is clearly paced by obliquity in the early period while the model appears to be paced by eccentricity in the later period. The system has one stable critical point before 1.2 myr of simulated time. Thus the pre-MPT phase pacing of the model to obliquity can be definitively categorized as phase locking to obliquity. That is to say, the model is correlated with the external forcing in such a way that there is a constant difference in the phase angle between the two oscillations. However, because the oscillations post-MPT in the simulated time are deviations from an unforced orbit which are also being affected by pseudo-quasi-periodic forcing, it is not intuitively obvious that the model is phase locking to eccentricity.

In this situation the circular statistics can be misleading. Because the model has so few cycles at 100 kyr, any correlation may be by chance. While this improved model is more in line with the observed δ^{18}O data, the model highlights a limitation of any dynamic Hopf bifurcation MPT model. That is, the phase correlation cannot be shown to be causal because there are too few observed cycles to compare to.

Both MS90 and MS90BSWM are quite complicated models. The original MS90 model from Equation 3.2 does not produce results similar to the δ^{18}O data. In this chapter a new model was presented which more realistically incorporates Milankovitch

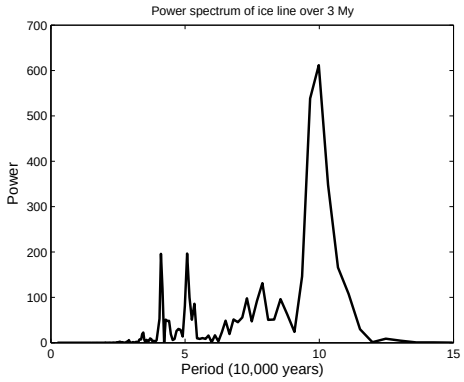

Figure 4.3: Fourier power spectrum of ice line values over the last 3 myr of simulated time.

forcing. But this new model also has many short comings. MS90BSWM shows a stronger 41 kyr signal before the MPT and correlation with eccentricity after the MPT. However, the model does not show a continued phase correlation with obliquity like the δ^{18}O does. It would be difficult to understand all the details of these models. In fact, our current mathematical understanding of dynamic Hopf bifurcations is limited enough that the mathematical tools are not developed enough to understand all the features in MS90 and MS90BSWM.

To add further intrigue, the model's phase angles show a strong sensitivity to initial conditions (see Figure 4.5). The model is complicated enough that there is no clear reason for the sensitivity. The sensitivity could be a local problem of timing against the quasi-periodic forcing terms or something more general. Despite the initial clustering of the solutions, once the system passed through the Hopf bifurcation, the solutions begin to diverge from one another. Rayleigh R phase angle statistics are sensitive enough that these shifts will change the correlation of the solution to the external forcing.

To understand the sensitivity of phase angle to initial condition and external forcing mathematically, a well understood model is introduced. Because very little research has been done in the field of quasi-periodically forced Hopf bifurcations, a well understood model will also be a less complex model. The model will simplify the relationship between the phase of the forcing and the phase of the model. By reducing the complexity of the problem, the natural connection between the phase angle of the model and the

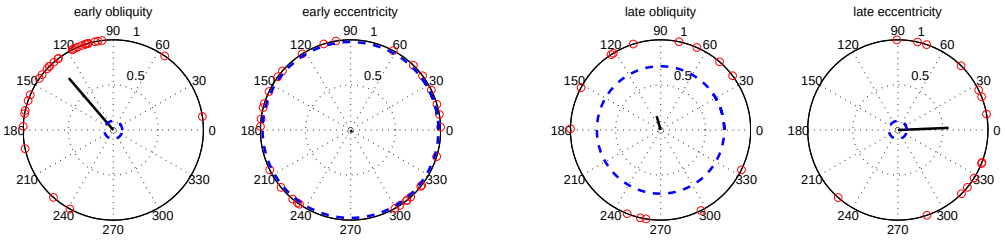

Figure 4.4: Rayleigh R phase angle analysis between model ice line output and orbital forcing for early (3 myr - 1.2 myr) and late (1.2 myr to present) Pleistocene. The reader is referenced to Zar (1999) and Upton and Fingleton (1989) for details on the circular statistics used to produce these diagrams as well as the explaination given in Chapter 3 [38, 39]. Lisiecki (2010) also presents a concise review of the process [13].

forcing will be highlighted. In the next chapter, a generalized forced oscillator with a dynamic hopf bifurcation will be described and analysed. In Chapters 5 and 6, arguments will be given to show when phase correlation can and cannot be predicted. In Chapter 7 the analysis will return to the MS90BSWM model to determine how well the conclusions of a two dimensional dynamic Hopf bifurcation forced oscillator model apply.

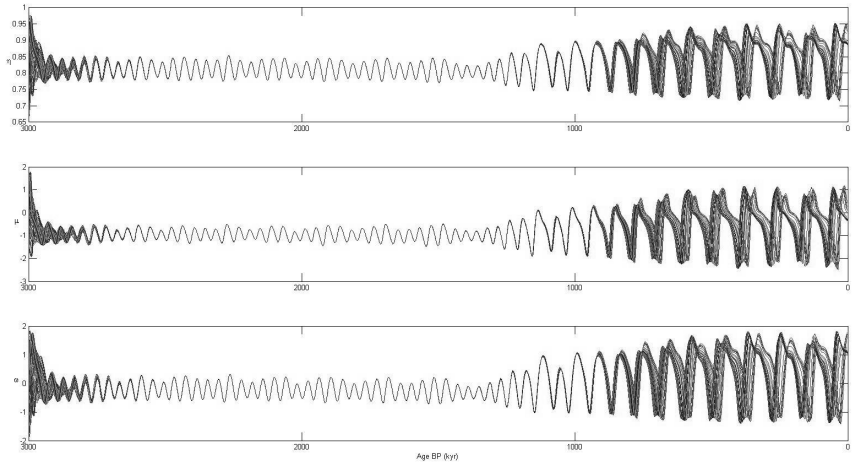

Figure 4.5: One example of the sensitivity to initial conditions of MS90BSWM. There are 64 different initial conditions: $\eta \in \{0.65, 0.75, 0.85, 0.95\}$, $\mu \in \{-1.5, -0.5, 0.5, 1.5\}, \omega \in \{-1.5, -0.5, 0.5, 1.5\}$. The model was numerically integrated for 3 myr of simulated time using the dynamic changes described in Table 4.2. Notice how, regardless of the contraction pre-bifurcation, the model runs with different initial conditions are quite different post-bifurcation.

Chapter 5

Generalized dynamic Hopf bifurcation analysis: McGehee and Peckham

5.1 The McGehee and Peckham Model

In order to formally question the assumption of phase angle correlation between the earth's fundamental formulation as a Hopf bifurcation and the external forcing, the model must be generalized and simplified. To simplify only one external forcing term will be considered. Only obliquity will be considered because obliquity appears to be the most dominant influence on the planet [8]. This chapter will consider the forced oscillator map with a Hopf bifurcation that is described in McGehee and Peckham (1994) [43]. The McGehee and Peckham model takes advantage of the periodic nature of the forcing term by being formulated as a discrete period map. Then, more generally, an analysis of the phase of the dynamic Hopf bifurcation will be presented by considering the phase plane plots of this map and improved versions of this map.

To perform a general study of Hopf bifurcations for forced oscillators, McGehee and Peckham use a Hopf bifurcation of maps which can be numerically analyzed on computers. $H_{(\alpha,\beta)} = g_\alpha \circ h_\beta$ is defined in McGehee and Peckham (1994). The map h_β

is taken from the time one map following the planar vector field:

$$\dot{r} = \frac{r(1-r^2)}{1+r^2} \qquad \dot{\theta} = 2\pi\beta + \frac{1-r^2}{1+r^2}.$$

Here, $\beta \in \mathbb{R}$ such that $\beta > 0$. This differential equation, which is written in polar coordinates can be solved using separation of variables. The map g_α is defined in the complex plane as:

$$g_\alpha(z) = (1-\alpha)(z-1) + 1.$$

Here $\alpha \in \mathbb{R}$ such that $\alpha > 0$. This can be easily translated into Cartesian coordinates for our purposes. The solution to the above equations written as a map (take $t = 1$) is as follows:

$$\begin{aligned} h_\beta = & \begin{cases} r_{i+1} = \frac{1}{2}\left(-ke^{-t} + \sqrt{k^2e^{-2t}+1}\right) \\ \theta_{i+1} = 2\pi\beta t + \theta_i + \frac{r_{i+1}^2 - r_i^2}{2}t \end{cases} \\ g_\alpha = & \begin{cases} x_{i+1} = x_i + \alpha(1-x_i) \\ y_{i+1} = y_i - \alpha y_i \end{cases} \end{aligned} \tag{5.1}$$

Please note: The h_β equation is in polar coordinates while the g_α equation is in Cartesian coordinates. This is done for clarity of communicating what each map does. For $\alpha = 0$, the unit circle is invariant with a rigid rotation with rotation number β. For $1 >> \alpha > 0$, the circle distorts but remains invariant. And for α near 1, there is only an attracting fixed point at $(x, y) = (1, 0)$. The parameter β is the rotation number of the invariant circle. The constant k is defined as $\frac{1-r_0^2}{r_0}$ where r_0 is the initial radius.

McGehee and Peckham consider the system numerically in a 4 dimensional space of the phase plane cross the parameter space. The authors analytically solve for resonance, or phase-locking, surfaces in the 4-D space. Then the resonance surfaces for $H_{(\alpha,\beta)}$ are projected onto the parameter space to produce the Arnold Tongue diagram in Figure 5.1. Thus the resonance ratio can be determined for which pair of α and β where resonance exists.

There are some limitations to the model in its current formulation. While the model considers a Hopf bifurcation map, the model is only capable of modeling the system post-bifurcation. In order to reproduce the dynamic bifurcation as seen in Chapters 3 and 4, the model must be adjusted.

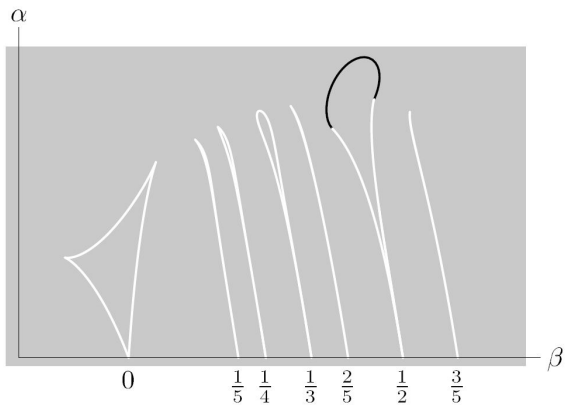

Figure 5.1: Arnold Tongue diagram showing regions of constant rotation number on the parameter plane of (β, α). This image is a reproduction with permission from McGehee and Peckham's 1994 paper [43].

5.2 Traditional Bifurcation Analysis and Results

In order to build on the work covered in Section 5.1, a dynamic Hopf bifurcation parameter must be introduced. The function, k_γ, will be added to the family of maps defined in McGehee and Peckham (1994) to include a Hopf-type bifurcation [43]. Thus the time one map (set $t = 1$) $G_{(\alpha,\beta,\gamma)} = g_\alpha \circ h_\beta \circ k_\gamma$ is as follows:

$$\begin{aligned} k_\gamma = & \begin{cases} r_{i+1} = r_i e^{(\gamma-1)t} \\ \theta_{i+1} = \theta_i \end{cases} \\ h_\beta = & \begin{cases} r_{i+1} = \frac{1}{2}\left(-ke^{-t} + \sqrt{k^2 e^{-2t} + 1}\right) \\ \theta_{i+1} = 2\pi\beta t + \theta_i + \frac{r_{i+1}^2 - r_i^2}{2} t \end{cases} \\ g_\alpha = & \begin{cases} x_{i+1} = x_i + \alpha(1 - x_i) \\ y_{i+1} = y_i - \alpha y_i \end{cases} \end{aligned} \tag{5.2}$$

Please note, the first two functions are written in polar coordinates and the last in Cartesian coordinates. The newly added map k_γ is a contraction of the domain towards the origin. For $\gamma = 1$, the map, $G_{(\alpha,\beta,1)} = H_{(\alpha,\beta)}$. For $1 > \gamma > 0$, the map k contracts towards the origin. For $\gamma \leq 0$, the model has one attracting fixed point at $(0, 0)$. Thus, γ will be the bifurcation parameter.

The fixed conditions of the model will be analyzed and then the dynamic Hopf bifurcation will be considered. By considering the output of the model on the phase

plane and the possible convergence of the map under different parameters, one can count the number of stable trajectories for a given set of parameters: (α, β, γ). This is computed numerically by studying the phase plane of the system. By mapping forward in time, clustering analysis can be used to show if the system is in a resonance region or not. For example, our planet has a period of 100 kyr and obliquity has a period of 41 kyr. This means the model should have $4:10$ or $2:5$ resonance to reproduce that found on Earth. This implies that the map must take 5 progressions before it lands in the same spot on the invariant manifold, see Figure 5.2. Thus 5 distinct clusters to exist in a resonance region of $2:5$ resonance ratio. This cluster analysis builds on the concept of stable trajectories.

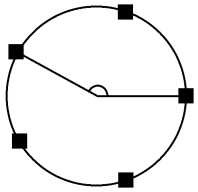

Figure 5.2: Diagram showing the five stable trajectories expected for a $2:5$ resonance. Each marker is $\frac{2}{5}^{\text{th}}$ of the way around the circle.

A stable trajectory is one for which the largest Lyapunov exponent, λ_{max}, is negative. The largest Lyapunov exponent, λ_{max} is mathematically defined as:

$$\lambda_{max} = \lim_{|\delta Z(0)| \to 0} \lim_{t \to \infty} \frac{1}{t} ln \frac{|\delta \mathbb{Z}(t)|}{|\delta \mathbb{Z}(0)|} \tag{5.3}$$

where $\delta \mathbb{Z} = [\delta x, \delta y]$ are vanishing perturbations around x and y [44]. De Saedeleer (2012) observed, "cluster analysis for paleoclimatic dynamics comes from the natural fact that clustering is another way of looking at general synchronisation where negative $[\lambda_{max}]$ makes the trajectories cluster more efficiently" [29]. In this paper a similar clustering algorithm is used to determine the Arnold Tongues and, thereby, the stable trajectories of a system. For Equations 5.2, the phase plane is analyzed using cluster techniques. By mapping a trajectory forward in time and organizing all the locations onto the phase plane, one can determine if the trajectory passes through the same location of the phase plane. If so, then the trajectory has a stable cycle that repeats every $40,000n$ years, where n is the number of distinct clusters of trajectories on the

phase plane. For further reading on stable trajectories of dynamic Hopf bifurcations, see De Saedeleer (2012) and Wieczorek (2012) which offers good insights into identifying and counting stable trajectories [29, 35].

By fixing a γ and testing each point in (α, β, γ) space an Arnold Tongue diagram can be produced for that fixed γ slice of the parameter phase space. Arnold Tongue diagrams were created for

$$\gamma \in \{-0.1, 0, 0.1, 0.2, 0.3, 0.4, 0.5, 0.6, 0.7, 0.8, 0.9, 1\}$$

and can be found in Figure 5.3. The bifurcation takes place at $\gamma = 0$, thus the Arnold Tongues grow as γ increased beyond zero. Recall that at $\gamma = 1$, the function $G_{(\alpha,\beta,1)} = H_{(\alpha,\beta)}$ from McGehee and Peckham (1994). The $\gamma = 1$ image is a more detailed version of the Figure 1 from the original publication, see Figure 5.4. [43].

To compare the results of the McGehee and Peckham model to our planet, a set of (α, β) such that the ratio of the natural frequency to the forcing frequency is $\frac{4}{10}$ must be chosen. This is because the largest forcing our planet receives is obliquity and the model has an internal 100 kyr cycle [16]. This is equivalent to a (α, β) pair for which the system has 5 stable trajectories. The point, $p_1 = (\alpha, \beta) = (0.40, 0.3775893)$, will be used for all future analysis. This point was chosen because it is near the middle of the Arnold Tongue where the α value is large enough to be of consequence, but not so large that the system is a slave to it.

Consider a trajectory simulated over 3 myr and 80 myr with constant $\gamma = 1$ by $G_{(0.4,0.3775893,1)} = F_{(0.4,0.3775893)}$. See Figure 5.5 to view the period maps of the simulations. Here, one can view the phase plane through time to visualize how the system converges to the stable trajectories. There are a few points on the trajectory scattered around the plane before the resonance is quickly realized. Then the system appears to converge to 5 stable points within the period map as early as 3 myr into the simulation. Within an 80 myr simulation the trajectory starts to migrate around the invariant curve. This suggests that the point p_1 might not be precisely on the $2:5$ resonance. However, for our purposes, the resonance is close enough to $2:5$ that, visually, the trajectories converge.

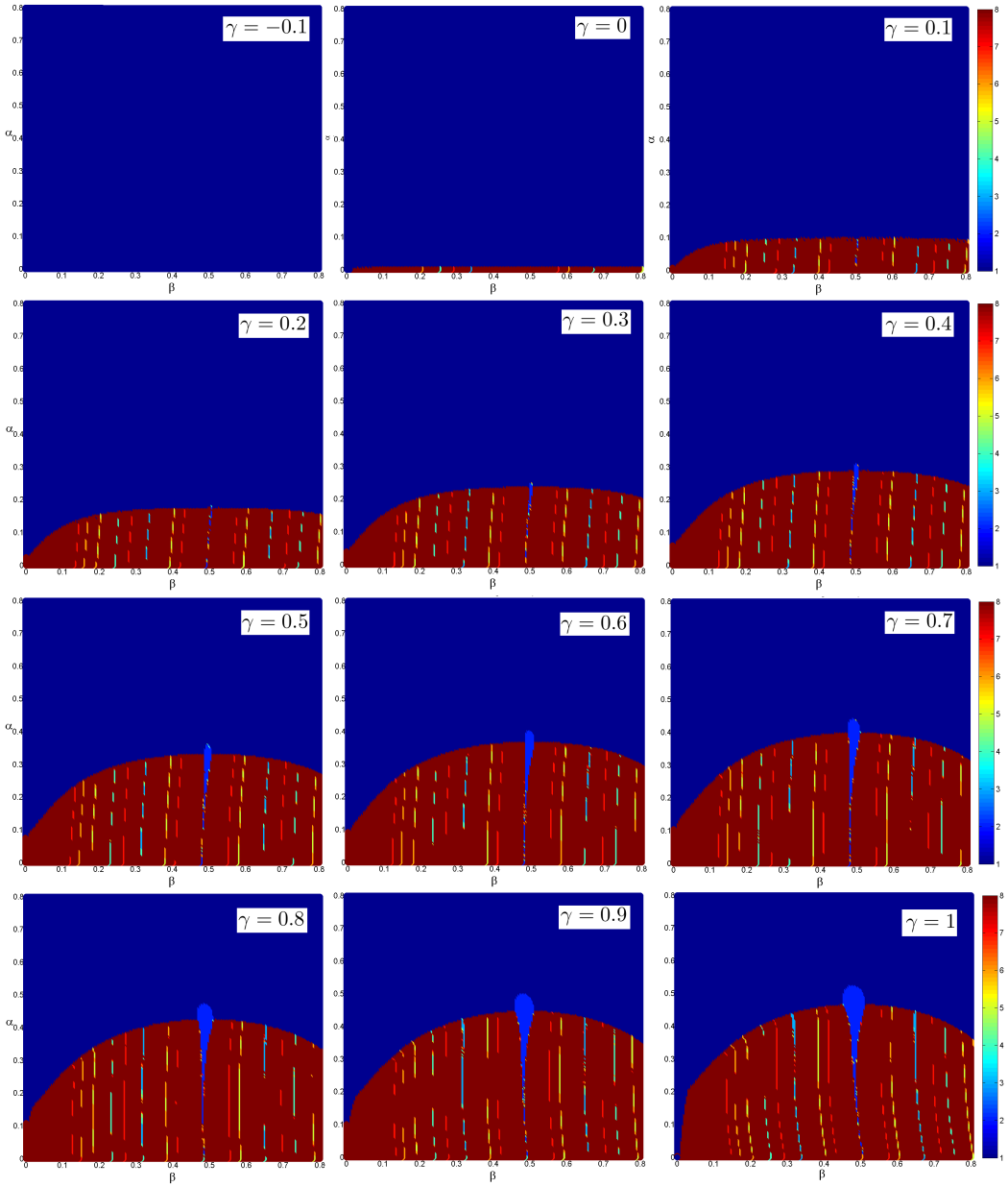

Figure 5.3: Arnold Tongue diagrams of $H_{(\alpha,\beta,\gamma)}$ for $\gamma \in \{-0.1, 0, 0.1, 0.2, 0.3, 0.4, 0.5, 0.6, 0.7, 0.8, 0.9, 1\}$. The Arnold Tongues grow as γ increased. Note that at $\gamma = 1$, the function $G_{(\alpha,\beta,\gamma)} = H_{(\alpha,\beta)}$ from the 1994 paper. Due to increased computing power for the last two decades, the $\gamma = 1$ image is a more detailed version of the Figure 1 from the original publication [43] and can be seen more clearly in Figure 5.4.

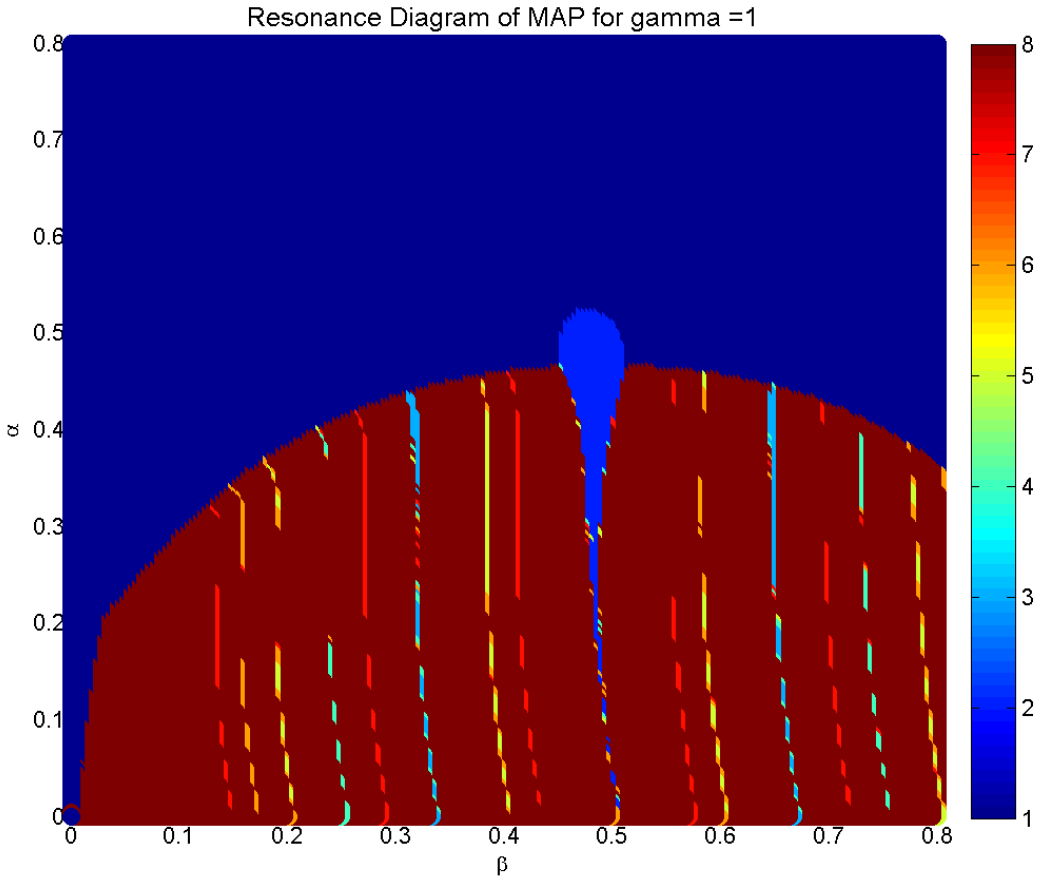

Figure 5.4: Arnold Tongue diagram for $\gamma = 1$. Note that at $\gamma = 1$, the function $G_{(\alpha,\beta,\gamma)} = H_{(\alpha,\beta)}$ from the 1994 paper. Due to increased computing power for the last two decades, the $\gamma = 1$ image is a more detailed version of the Figure 1 from the original publication [43].

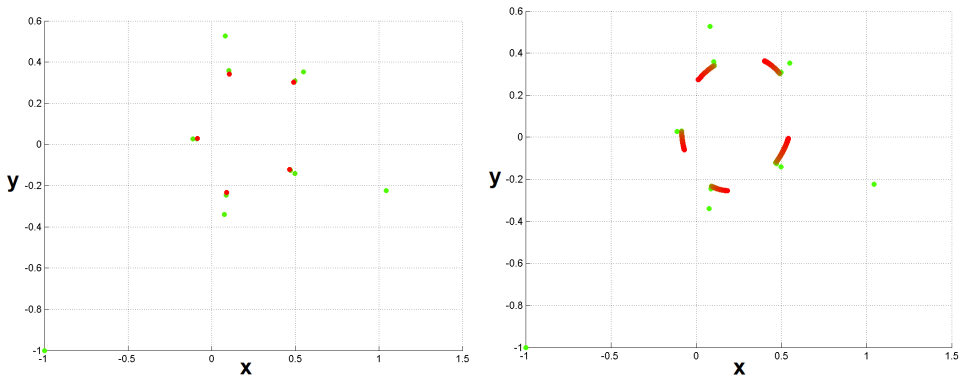

Figure 5.5: Period map of classic McGehee and Peckham model: $H_{(\alpha,\beta)}$ for a simulated time of 3 myr (left) and 80 myr (right) with $\alpha = 0.4$ and $\beta = 0.3775893$. Here, one can view the phase plane through time to visualize how the system converges to the stable trajectories. Earlier times are lighter and later times are darker. The system converges to the five stable orbits where the dots converge.

5.3 Dynamic Bifurcation Analysis and Results

Now the model will be analyzed for a dynamically changing γ. Dynamic bifurcation literature states that if the dynamic variable is changes slowly enough, the qualitative aspects of the system are similar to those found in the traditional bifurcation analysis. For this analysis, define $\gamma = 0.1$ at the beginning of the model time, then slowly change γ to 1 over the first 1 myr, and finally stabilize at $\gamma = 1$ for the later part of the simulation. By considering the Arnold Tongue diagram at $p_1 = (\alpha, \beta) = (0.4, 0.3775893)$ one can notice that this change in γ begins before the bifurcation and ends in the resonance tongue of $2 : 5$. In fact, when simulating $G_{(p_1,\gamma)}$, the model yields similar results to those shown in Figure 5.5, so the period map for dynamic γ will not be included here.

Many initial conditions will be considered in these simulations. Each of these initial conditions will produce its own trajectory. For ease of discussing trajectories, each trajectory is identified by its initial conditions. Because the system is completely deterministic[1] , the initial condition is a reasonable identifier. Define the trajectory from

[1] This statement is accurate modulo some computer precision error. As will be discussed, trajectories are very sensitive to initial conditions. During the testing process, contradicting and unreproducible results showed that computer precision round off error was capable of producing erroneous results. By considering a grid of initial conditions and testing that the results are reproducible, the effect of computer precision round off errors is minimized (but not eliminated).

initial condition (x_1, y_1) as:

$$T_{(x_1,y_1)} = \left\{(x,y)|(x,y) = G_{(\alpha,\beta,\gamma)}(x_1, y_1, t)\ \forall\ t \in [0,\infty)\right\}$$

The initial conditions will be a grid of 441 points for values of x and y between -1 and 1 with a distance of 0.1 between points. Figure 5.6 shows the time series of the simulation for a 3 myr simulation. Based on the Arnold Tongue diagram and the period maps presented in Figure 5.5, the system should have exactly 5 stable trajectories. The period map is not the best visualization tool for identifying the phase of a particular trajectory. This is because the time data has been hidden. By considering the time series, the phase information of the simulation can be recaptured. Note, one time step in $G_{(\alpha,\beta,\gamma)}$ represents $40,000$ years of simulated time. Thus, the time series has a very coarse resolution. However, $G_{(\alpha,\beta,\gamma)}$ is well understood map which solves each differential equation individually. Thus, a solution, however coarse, can be seen as a reasonable representation of the original differential system. By considering the time series, the phase angles of each trajectory are easily distinguished from one another.

In the case of the 3 myr simulation presented in Figure 5.6, the model was not simulated for sufficient time steps to allow the model to converge completely. That is to say, if the model has $2:5$ resonance there will be an invariant curve which is topologically equivalent to a circle with 5 stable points and 5 unstable points, see Figure 5.7.

In fact, the collection of 441 initial conditions do converge to exactly 5 stable trajectories. Figure 5.8, presents the last 1 myr of a 80 myr simulation of $G_{(\alpha,\beta,\gamma)}$. There are exactly 5 stable orbits onto which all 441 trajectories must converge. This suggest the max lyapunov exponents of the system are weak. This is exactly what the Arnold Tongue diagram suggests for $(\alpha, \beta) = (0.4, 0.3775893)$. The trajectories are mostly realized by 30 myr of simulated time. This example was run until the trajectories were very highly clustered.

For the above analysis, only visual analysis was used to interpret the results to show that, indeed, there are 5 distinct trajectories which move between the 5 periodically stable points on the phase plane. Beyond a visual analysis, one can be more thorough in the analysis of initial conditions. By categorizing a grid of initial conditions based on which stable trajectory that initial condition converges to post-bifurcation, $\mathbb{R}^2$ can be partitioned into regions. The basin of attraction are determined for each stable periodic

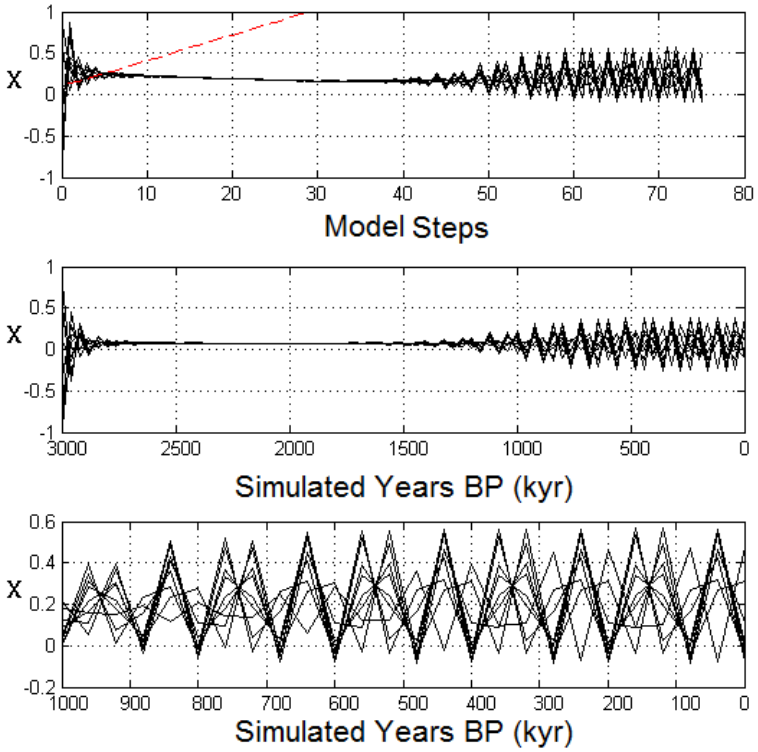

Figure 5.6: Time series for 441 initial conditions of $G_{(\alpha,\beta,\gamma)}$. For this run $(\alpha, \beta) = (0.4, 0.3775893)$, γ dynamically changes linearly from 0.1 to 1 over the first 1 myr of simulated time. The initial conditions are spread from -1 to 1 in both variables with a distance of 0.1. The dashed line shows the value of γ over the run. The top graph show the x value of the model with respect to model steps. Thus 75 model steps correlate to 3 myr of simulated time. The middle graph shows the y value of the model with respect to simulated time as though the initial time was 3 myr ago. The bottom graph presents a close up of the last 1 myr. The trajectories converge before the bifurcation and diverge into many separate trajectories after the bifurcation takes effect.

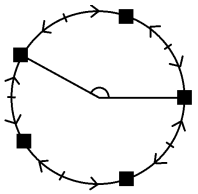

Figure 5.7: Diagram of stable and unstable points on the invariant curve. The trajectories of any initial condition will converge to these 5 stable points on the periodic map of the phase plane.

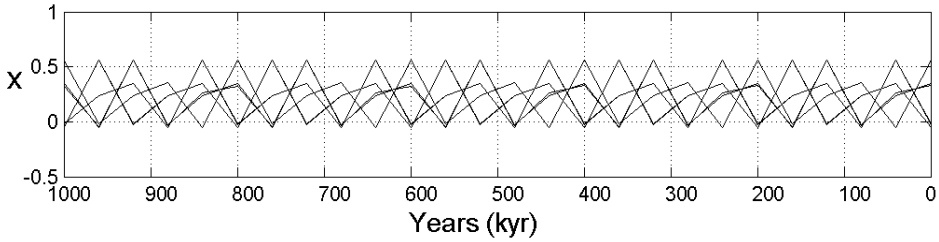

Figure 5.8: Final 1 myr of 80 myr simulation of $G_{(\alpha,\beta,\gamma)}$ with 441 initial conditions. Notice there are exactly 5 trajectories visible in this graph. This is because the initial conditions have all converged close enough to the stable trajectories of the system that only 5 trajectories appear in the plot. This is exactly what the Arnold Tongue diagram suggests for $(\alpha, \beta) = (0.4, 0.3775893)$.

trajectory as follows:

For a given (α, β) there exist n convergence points on the phase plane as determined by the Arnold Tongue diagram. Given an initial condition $(\hat{x}, \hat{y})$, integrate to find $T_{(\hat{x},\hat{y})}$ for a predetermined number of simulated years. Next, determine the (x, y) values of the last peak of simulated $T_{(\hat{x},\hat{y})}$. Identify which convergence point on the phase plane the last peak of $T_{(\hat{x},\hat{y})}$ is closest to by checking a closeness criterion. The closeness criterion is satisfied if the Euclidian distance is less than some small threshold. For this analysis, a threshold of 0.2 was chosen. Finally, $(\hat{x}, \hat{y})$ is assigned the value associated to the nearby convergence point. Thus, initial condition are coded based on the relative phase of $T_{(\hat{x},\hat{y})}$.

To apply this analysis, consider a model run of 30 myr. Figure 5.9 shows the grid of 441 initial conditions coded by which stable trajectory the $T_{(\hat{x},\hat{y})}$ converges to. The figure also presents the final position of the initial conditions along the invariant curve. Because

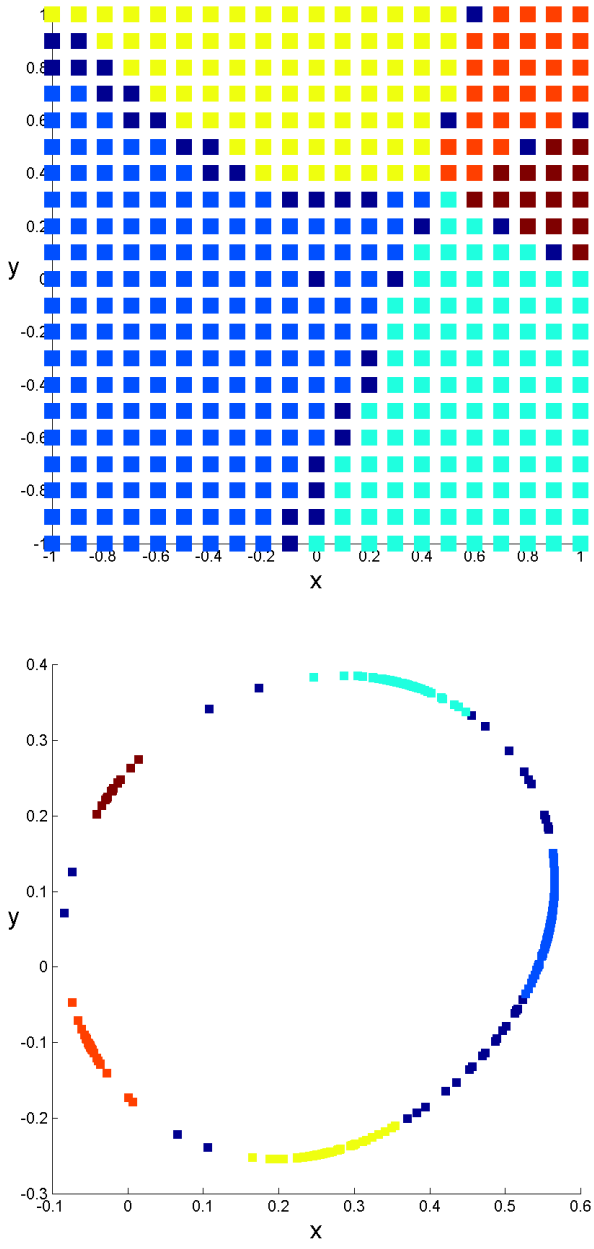

Figure 5.9: Initial (top) and final (bottom) positions of 441 trajectories of $G_{(\alpha,\beta,\gamma)}$ coded by final position.

the trajectories have not converged completely there are a few initial conditions that are not coded to a particular trajectory. These unclassified initial conditions may all be classified if the model is simulated for sufficiently many time steps such that the model converges to the stable trajectories more closely. The initial condition classification has a clear spiral structure. This analysis shows that the structure of the organization of initial conditions persists as the trajectories move through the bifurcation. In fact, if the bifurcation is run over a long time frame, five stable trajectories are more obvious. This phenomenon can be understood with manifolds. Figure 5.10 shows a diagram of the manifolds of the dynamic Hopf bifurcation. It is reasonable that if there are 5 stable points on the final invariant curve, then there are also 5 unstable points. The preimages of those unstable points are the boundaries between the basin of attraction shown in Figure 5.9. If the system is allowed to converge to one trajectory before the bifurcation then the system will stay on a single trajectory after the bifurcation. Thus, for a dynamic γ and an array of initial conditions the trajectories of $G_{(\alpha,\beta,\gamma)}$ may be fully understood.

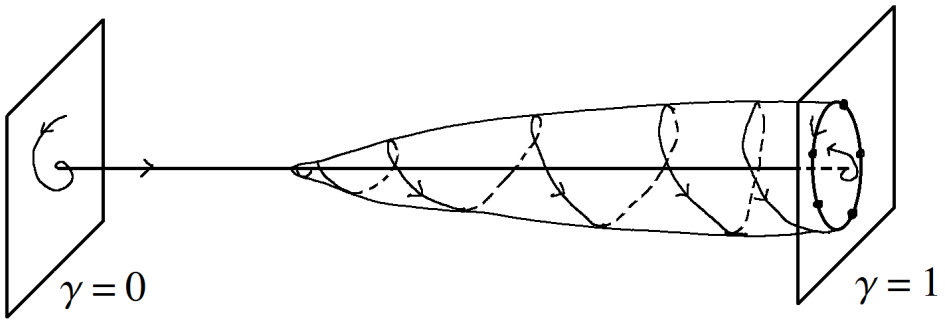

Figure 5.10: Diagram of dynamic Hopf bifurcation manifolds. Each trajectory will begin its path by collapsing towards the equilibrium point. If it does not converge completely, then it will diverge to a well determined stable trajectory post-bifurcation.

Now that a solid mathematical footing for the deterministic, dynamic Hopf bifurcation, time one map, $G_{(\alpha,\beta,\gamma)}$ has been determined, the original problem of phase angle statistics remains. In Chapter 6, a finer version of the map is created so the phase angle of a trajectory and the external forcing may be considered. The McGehee and Peckham model will also be analysed after stochastic noise is added in the next chapter.

Chapter 6

Generalized dynamic Hopf bifurcation: Finer forced oscillator map

In this chapter the mathematical framework presented in Chapter 5 will be expanded. First the effects of noise on the dynamic version of the McGehee Peckham model, $G_{(\alpha,\beta,\gamma)}$ will be considered. In the latter half of the chapter the original problem of phase angle statistics discussed in Chapter 3 and 4 will be revisited.

6.1 Adding Noise to $G_{(\alpha,\beta,\gamma)}$

No system exists in a vacuum, and so the system must be considered with noise. To consider the mathematical results found in Chapter 5 as a predictor of climate, one must know how robust the model is to noise.

Thus stochastic noise with normal distribution with mean 0 and standard deviation of 0.01 will be added. The stochastic noise will be added to the model $G_{(\alpha,\beta,\gamma)}$ in the x direction at the beginning of each time step. The system still shows distinct clustering to 5 stable trajectories for an individual run (not shown). Thus, one might expect the grid of 441 initial conditions to cluster to 5 stable period points on the phase plane as well. And they do. However, the pre-images of the clusters, or the basin of attraction

for each stable cluster, have no clear structure. In fact, the pre-image of a specific stable trajectory appear to be randomly spread amongst the initial conditions. Figure 6.1 shows the initial conditions and final clustering.

This shows that a noisy Hopf bifurcation will not allow for the prediction of the phase of a trajectory based on its initial condition. The author believes that there is a relationship between noise and the radius of the trajectories at the narrowest moment of the bifurcation neck (which has to do with the absolute value of the real part of the eigenvalue of the stable equilibrium, the length of time over which the bifurcation parameter is changed, and the radius of initial conditions from the stable fixed point). If the noise is large enough to push a trajectory from one stable manifold to another, then the phase will not be predictable. For example, if a system spends longer collapsing to a stable fixed point, a smaller amount of noise is necessary to change the basins of attraction. Further analysis is needed to determine the exact relationship described here. But, fundamentally, any small amount of noise could put a trajectory near the center of the spiral structure seen in Figure 5.9 to a different basin. The added noise that created the results in Figure 6.1 was large enough that initial conditions within radius of at least 1 from the fixed point were disrupted.

Despite the elegant structure of the dyanmic Hopf bifrucation illuminated in Chapter 5, the addition of noise removes the possibly of predicting phase angle meaningfully. In Chapter 7 noise will be added to the MS90BSWM model and analyzed.

6.2 Finer Model Formulation

The time series plots in Figure 5.6 and 5.8 from Chapter 5 are poor interpretations of the time series of the system because $G_{(\alpha,\beta,\gamma)}$ only produces information once every 40 kyr of simulated time. To truly visualize the system's time series, a period map with a smaller period must be constructed such that it is equivalent to the 40 kyr period map of the McGehee and Peckham every 40 kyr.

The new formulation of $H_{(\alpha,\beta,\gamma)}$ is Equation 5.2. This new model is $F_{(\alpha,\beta,\gamma,\sigma)} =$

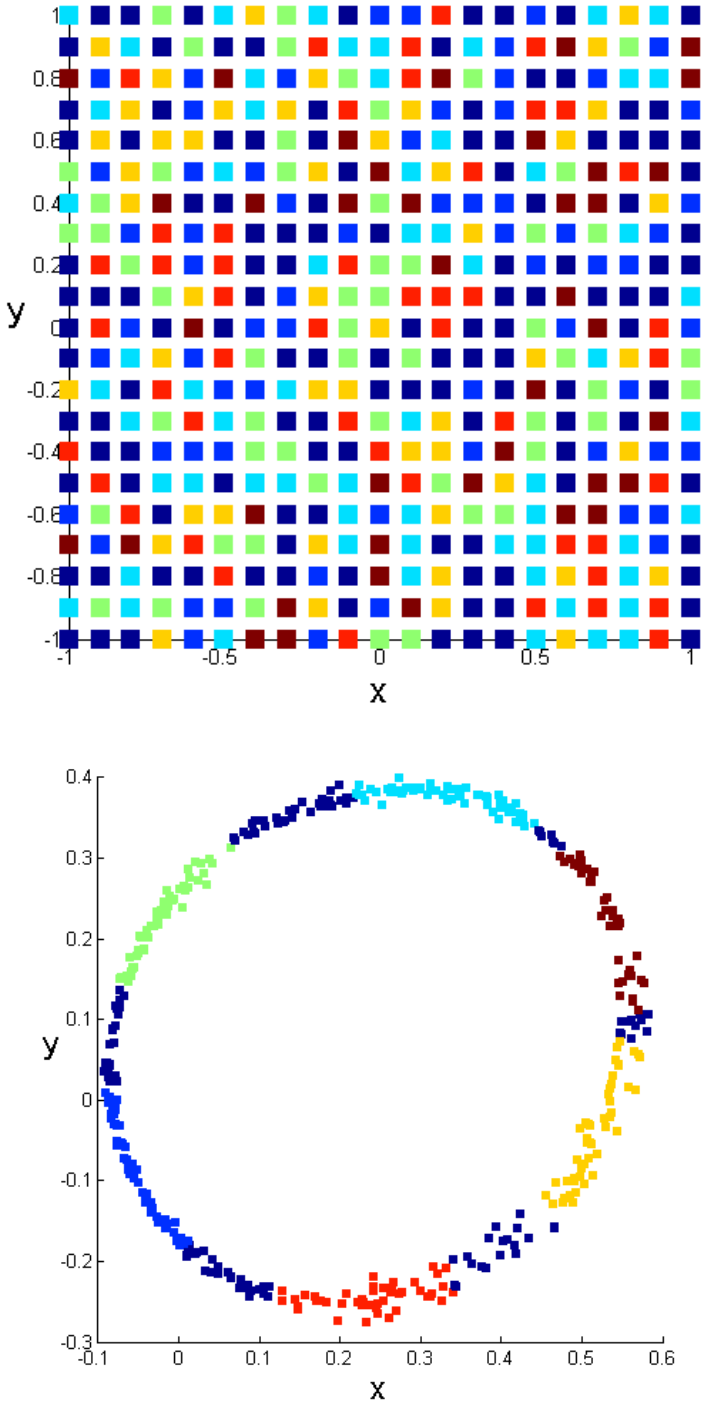

Figure 6.1: Initial (top) and final (bottom) positions of 441 trajectories of $G_{(\alpha,\beta,\gamma)}$ with stochastic noise coded by final position.

$f_\sigma \circ k_\gamma \circ h_\beta \circ g_\gamma$ where f_σ, k_γ, h_β, g_γ are defined as the following map:

$$
\begin{aligned}
f_\sigma = &\begin{cases} x_{i+1} = x_i \\ y_{i+1} = y_i e^{\sigma t} + M(t) \end{cases} \\
k_\gamma = &\begin{cases} r_{i+1} = r_i e^{(\gamma-1)t} \\ \theta_{i+1} = \theta_i \end{cases} \\
h_\beta = &\begin{cases} r_{i+1} = \frac{1}{2}\left(-ke^{-t} + \sqrt{k^2 e^{-2t} + 1}\right) \\ \theta_{i+1} = 2\pi\beta t + \theta_i + \frac{r_{i+1}^2 - r_i^2}{2} t \end{cases} \\
g_\alpha = &\begin{cases} x_{i+1} = x_i + \alpha(1 - x_i) \\ y_{i+1} = y_i - \alpha y_i \end{cases}
\end{aligned}
\tag{6.1}
$$

where f_σ reintroduces the variation which takes place on time scales smaller than 40 kyr, the time between each period map of $H_{(\alpha,\beta,\gamma)}$. For this model, the map will be solved for $t = 0.025$ which is equivalent to 1 kyr of simulated time. Please note that f_σ and g_α are written in Cartesian coordinates while k_γ and h_β are written in polar coordinates. Obliquity cycles $\mathcal{M}(t)$ are simplified to be a sinusoidal function with period 40 kyr. Thus, $F_{(\alpha,\beta,\gamma,\sigma)}$ can be used to create a time series which correlates exactly with $H_{(\alpha,\beta,\gamma)}$ every 40 kyr (See Figure 6.2).

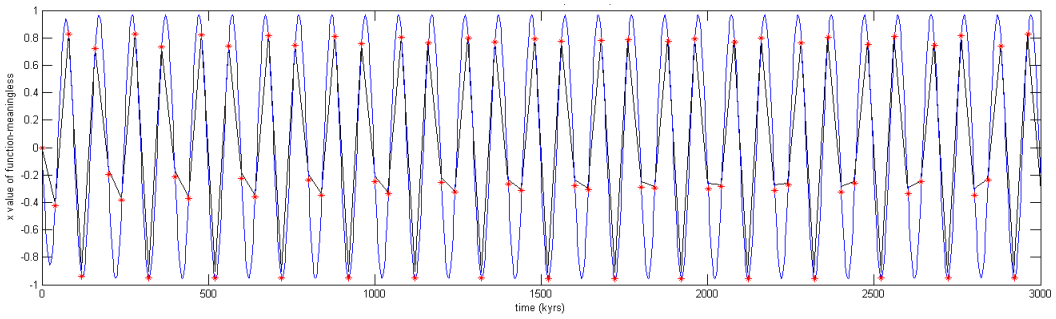

Figure 6.2: The model $F_{(\alpha,\beta,\gamma,\sigma)}$ produces a smooth curve through time. The straight lines connect the values of $H_{(\alpha,\beta,\gamma)}$ which exist only at each 40 kyrs. This image shows that $F_{(\alpha,\beta,\gamma,\sigma)}$ creates a time series which correlates exactly with $H_{(\alpha,\beta,\gamma)}$ every 40 kyr. The parameter values used here are $(\alpha,\ \beta) = (0.04, 0.39)$ and $\gamma = 1$. Because there is no change in γ, this run does not directly correlate to Earth and as such the x-axis is given as increasing simulated model years instead of Age BP. The stars highlight the locations in time where the period map is defined. It is clear that F fills in the gaps of the time series which H was designed to skip over.

For the comparison in Figure 6.2, a small value of α is used. For larger values of α the finer map will not approximate the coarse version as closely. This is reasonable because the maps within $F_{(\alpha,\beta,\gamma,\sigma)}$ do not commute [43]. So there is not a perfect analogue to the system presented in Chapter 5 nor to the differential equation version of the system $H_{(\alpha,\beta)}$ was based on.

The finer version of H, F, is integrated to recreate the analysis shown in Chapter 3 and 4 in a more standard way [10, 13, 14].

Figure 6.3 shows the trajectories of two initial conditions $(-0.01, 0.01)$ and $(-0.01, -0.01)$ which are close together for $(\alpha, \beta) = (0.04, 0.39)$ as defined in Chapter 5. $T_{(-0.01,0.01)}$ and $T_{(-0.01,-0.01)}$ are in phase with each other before the bifurcation and yet, after the bifurcation, they diverge to separate stable trajectories of the system. The figure also shows where the peaks of each trajectory relate to the phase of the external forcing. This is one example of how the final phase angle correlation of a trajectory in a dynamic Hopf bifurcation to its external forcing is sensitive to initial conditions.

6.3 Dynamic Hopf Phase Angle Conjectures

The work completed up to this point has been experimental in nature. The body of work presented thus far lends itself to a few conclusions that have yet to be carefully stated. This section will provide some technical conjectures which the author puts forward for further future inquiry. First, two conjectures are stated.

Conjecture 1. Given an initial condition, (x, y), and a dynamic Hopf bifurcation with constant parameters $p \in \mathbb{R}^n$ and dynamic parameter γ. If, for a given p, γ_{final} yields a system state for which multiple stable trajectories exist then there exist open, connected regions that are the pre-image of the stable trajectories.

Conjecture 2. With the hypothesis of Conjecture 1 and the addition of stochastic noise, there exists a function that incorporates:

1. the strength of the initial stable fixed point, x_{fixed}
2. the strength of the noise
3. the length of time over which the dynamic bifurcation occurs

to determine the radius of uncertainty, r_{crit}. That is to say, for $x \in B_{r_{\text{crit}}}(x_{\text{fixed}})$, the final phase of T_x cannot be known a priori.

The above conjectures are mathematical in nature and not obviously applicable to the question of the $100,000$ year problem of the MPT. Assuming these conjectures can be rigorously proven, several statements can be made about Earth's climate. Chapter 7 contains the discussion of applications to climate models.

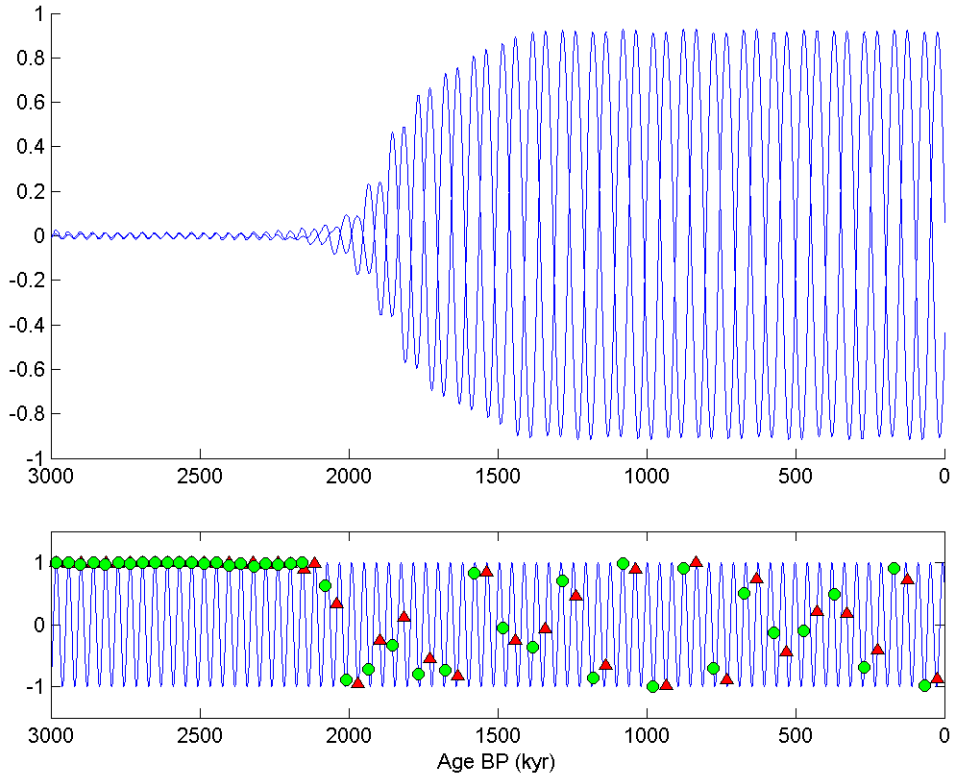

Figure 6.3: This figure shows $T_{(-0.01,0.01)}$ and $T_{(-0.01,-0.01)}$ which are on the same stable trajectory pre-bifurcation and converge to separate stable trajectories post-bifurcation. The figure also shows (circles and triangles) where the peaks of each trajectory correlate to the phase of the external forcing. This is one example of how the final phase angle correlation of a trajectory in a dynamic Hopf bifurcation to its external forcing is sensitive to initial conditions.

Chapter 7

Discussion of Application to Climate Models

Now that mathematical theories about the behavior of periodically forced oscillators containing dynamic Hopf bifurcations have been examined, our climate application awaits. This chapter will investigate the MS90BSWM model through the lens of stable trajectories developed in Chapter 5 and 6 to try to better understand the questions raised in Chapter 4.

7.1 Considering MS90BSWM with periodic forcing

To most directly apply the lessons of Chapter 5 and 6, MS90BSWM will be considered with the same type of forcing that was used in Chapter 6. In Chapter 6, the model is forced with orbital values of eccentricity and obliquity. For the first attempt at application, eccentricity values will be held constant so that Q has a constant value of 343 and obliquity will be defined as a sinusoidal function:

$$\beta = \sin(\frac{2}{41}\pi t + \frac{5\pi}{8}) + 23.3369.$$

Results of a 3 myr simulation are presented in Figure 7.1. Notice that model trajectories still seems to converge to a single stable trajectory before the bifurcation. Yet the model trajectories still diverges to multiple trajectories post bifurcation. This phenomena was also seen in Figure 4.5.

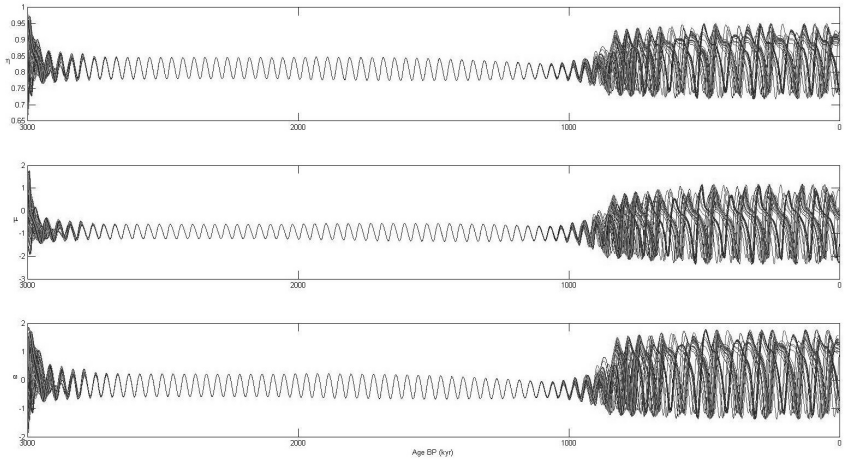

Figure 7.1: MS90BSWM model with periodic forcing in obliquity and constant eccentricity. The model was numerically integrated for 3 myr of simulated time using the dynamic changes described in Table 4.2.

If the theories of Chapter 6 apply, the single stable trajectory will actually be several different trajectories which are tightly packed. A $2:5$ resonance should be present and 5 stable trajectories will exist. To check this the system is run for another 6 myrs into the future to allow the system to converge to the stable trajectories. Figure 7.2 shows the last 1 myr of the 9 myr run. Visually there are two main trajectories which are more stable than others, but closer inspection may allow us to visually cluster the remaining trajectories. Figure 7.3 shows a 250 kyr section of the results in Figure 7.2.

More structure emerges in the last 250 kyr segment of the periodically forced model simulation. Because MS90BSWM is solved as a differential equation and not a map, fewer initial conditions may be considered at one time. This 9 myr run was completed with 64 initial conditions which is paltry compared to the 441 initial conditions which were tested with the McGehee Peckham map. This means that a trajectory cluster with 2 or 3 trajectories in it may be a legitimate stable trajectory. With this in mind Figure 7.3 presents a count of the number of trajectory clusters which appear. With a bit of creativity, 5 trajectory clusters can be counted. This is in line with the analysis from Chapter 6.

Please note: The creativity referred to in the previous paragraph may be mathematically appropriate because these trajectories are very sensitive to initial conditions.

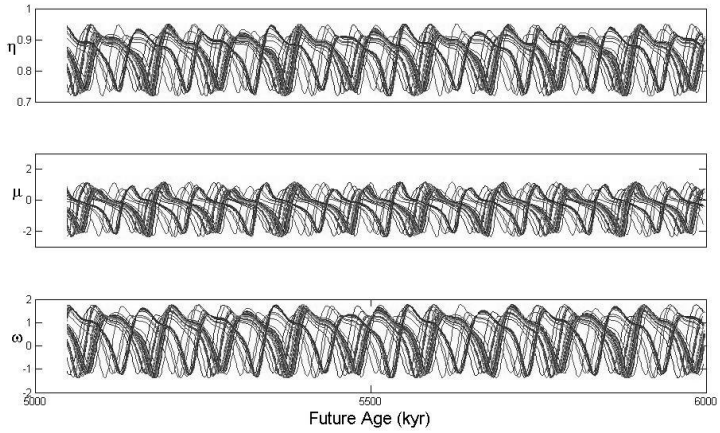

Figure 7.2: MS90BSWM model with periodic forcing in obliquity and constant eccentricity. This is the last 1 myr of 9 myr model integration. Thus the graph covers 5 to 6 million years in the future.

During the testing process, contradictory and unreproducible results showed that computer precision round off error was capable of producing erroneous results. By considering a grid of initial conditions and testing that the results are reproducible, the effect of computer precision round off errors is minimized (but not eliminated). The trajectory clusters seen in Figure 7.3 may also be viewed as 5 clusters at several time intervals and multiple model runs- so this *rough* categorization seems to be robust.

Comparing Figure 7.1 to Figure 4.5 offers interesting insights about dynamic Hopf bifurcations. The difference between these model runs is the use of Milankovitch obliquity and eccentricity versus a constant eccentricity and periodic obliquity. Initially some easily understood differences can be seen. Before the bifurcation in both systems, the trajectories all seemingly converge to one trajectory. In the periodic case, that trajectory is very sinusoidal while the qausi-periodically forced system produces a quasi-periodic solution. This is reasonable because the unforced system is converging to a single stable fixed point and so any oscillation is just reflecting the external forcing.

But some differences between 7.1 and Figure 4.5 are less understandable. Figure 4.5 shows that system spends longer near one trajectory post-bifurcation before diverging to multiple trajectories than the periodically forced system. The periodic forcing causes

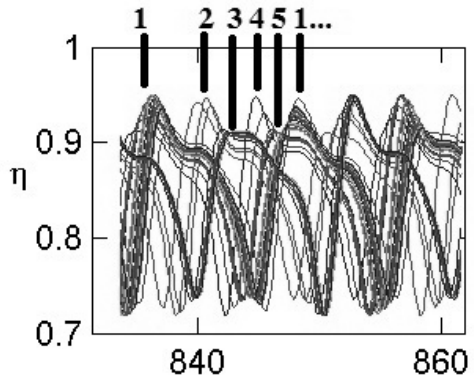

Figure 7.3: Left: MS90BSWM model with periodic forcing in obliquity and constant eccentricity. This is a 250 kyr segment from the last million years shown in Figure 7.2. It may be possible to count 5 stable trajectories. This may be a situation where the $41 : 105$ resonance is close to $2 : 5$ but not precisely resonating. Thus the theories of Chapter 6 with regard to stable trajectories may still apply to a 3 dimensional system.

the trajectories to diverge faster and with higher variance of phase angle after the bifurcation. So why does periodic forcing create divergent behavior when quasi-periodic forcing does not? Perhaps the quasi-periodic forcing overrules any small ratios of resonance. The system may not have a simple $2 : 5$ resonance. And as a result, the system will converge to many trajectories and give the impression of having higher variance in phase angle.

Both integrations in Figure 7.1 and Figure 4.5 have no stochastic, or noise, forcing. However, a minimal complexity model does not accurately represent the whole Earth system. Many of the processes on the planet are chaotic and will add noise to the system. Thus, as in Chapter 6, one must consider whether or not the model is robust to noise. Figure 7.4 shows a 9 myr run of MS90BSWM with obliquity forcing as a stochastic noise added at each time step. The stochastic noise is of normal distribution with standard deviation equal to 0.01. This is 0.05% of the total range $(-2, 2)$ of the system. The forcing is added to the η differential equation and is unique to each initial condition.

The clustering of the trajectories is truly remarkable. Without stochastic noise, the

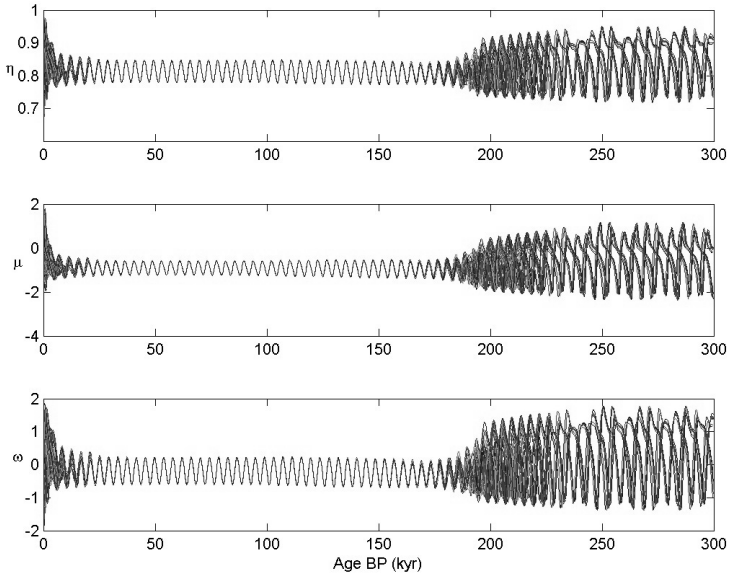

Figure 7.4: MS90BSWM with periodic obliquity forcing and stochastic noise. The stochastic noise has normal distribution around 0 with a standard deviation of 0.01. This is 0.05% of the total range of the system. The forcing is added to the η differential equation and is unique to each initial condition.

trajectories clustered to 5 or no groups, depending on how you classify a trajectory cluster. With stochastic noise the trajectories appear to converge to 2 or 3 clusters. This phenomenon is impressive and there is no current mathematical theory to help explain it. Suffice to say, the model is not robust to noise and the system changes significantly in a qualitative way when noise is added.

There are some differences between the climate model, MS90BSWM, and the McGehee Peckham model. MS90BSWM was treated as a system of differential equations while the McGehee Peckham model is a system of maps which closely resemble the period map of the associated differential equations. The climate model is also crafted in three variable dimensions while the McGehee Peckham model has only two variable dimensions. Thus there are some confounding factors that restrict our ability to generalize from the analysis on the McGehee and Peckham model to the work of Saltzman and

subsequent extensions of that work presented in Chapter 4. However, some broad discussion may still be made about the choice of using a dynamic Hopf bifurcation to model the mid-Pleistocene transition.

7.2 Climate Applications

Extending this mathematical work to climate applications is a tricky business. If climate conclusions may be extrapolated from the conjectures presented in Chapter 6, then one grand claim may be made about our planet's δ^{18}O data. That is, if the Earth's underlying structure is a Hopf bifurcation akin to those presented in this work, then the phase of the planet's recent 100 kyr cycles has no meaningful relationship to the external forcing. However, there are many implicit assumptions about the Earth which must be made before the results of this model can be applied to Earth's climate. To apply the mathematical inquiry of this work to Earth's climate, one must assume that the planet has a $\frac{4}{10}$ resonance with the external forcing. As discussed in Chapter 2, this is a reasonable assumption. Then it is the case that there are 5 stable trajectories our planet may converge to. Some of these trajectories will show a correlation with the external forcing and some will not. See Chapters 3 and 4 for a few examples of how a dynamic Hopf bifurcation model of the mid-Pleistocene transition can produce output which is in-phase and anti-correlated with the external forcing. As is the case with the initial examples, specifically that of Chapter 4, an accurate accounting for Milankovitch cycles does not reduce or eliminate the initial condition sensitivity. The sensitivity to initial conditions is a trait associated with the dynamic Hopf bifurcation and not the type or application of external forcing. In Chapter 6, the phase angle of a stable trajectory of a dynamic Hopf bifurcation was shown to be sensitive to initial conditions.

As an prelude to the conclusion, I present a thought experiment:

To show that Earth can be well modeled by a dynamic Hopf bifurcation, the following features must be investigated:

1. One must identify an internal cycle on the planet that has exactly 100 kyr period. At this time there does not seem to be any evidence for such a cycle in the

biosphere, cryosphere, hydrosphere, or atmosphere.

2. One must also show that after the Earth system underwent the Hopf bifurcation that there exists a stable trajectory which correlates to the external forcing and that T_{Earth} landed on that trajectory. This would be a cosmic coincidence with a small probability. Further mathematical investigation needs to be done to show such an event can be achieved with a Hopf bifurcation.

3. Despite the stochastic and chaotic features of the planet, one must further show that T_{Earth} has not moved from one stable trajectory to another over the last 1.2 myr. The model in Chapter 5 was shown to have very weak Lyaponov exponents, thus the stable trajectories are very weakly stable. This suggests that a trajectory may be pushed from one stable trajectory to another if relatively weak stochastic noise is applied to the system.

4. For the Hopf bifurcation model to be predictive, the noise associated to Earth's climate must be shown to be below some critical threshold. If the noise associated with climate is too large then phase predictions cannot be made.

While these events may be possible, the probability of all of these statements being true is quite small. Thus the author of this dissertation believes it is reasonable to assume that the planet does not have the underlying structure of a Hopf bifurcation. [1]

[1] Please note: the work in this thesis falls short of proving the corollary. I have only addressed a sinusoidal external forcing function.

Chapter 8

Conclusion

Classic dynamic Hopf bifurcation models are insufficiently reproducing the current understanding of the δ^{18}O data. Hopf bifurcations have a structure that allows a trajectory to have a certain phase with relation to the external forcing, up to a point. There are only a finite number of possible relationships a trajectory may have against the external forcing based on the resonance of the system. So, with deterministic analysis, the Hopf bifurcation seems like a reasonable choice. However, with the addition of a small amount of stochastic noise, the pre-image of the stable trajectories lose their structure. As a result, it is likely that the post-MPT phase angle results cannot be predicted for a dynamic Hopf bifurcation model. It is a matter of chance and choice of initial condition that the model results will be in phase with the external forcing in the same way as the δ^{18}O data is with the Milankovitch cycles. The work presented here strongly suggests that a dynamic Hopf bifurcation will not successfully model the mid-Pleistocene transition. Dynamic Hopf bifurcations provide a rich field for mathematical inquiry. However, as the understanding of the δ^{18}O data and of dynamic Hopf bifurcations increases, the Hopf bifurcation models decrease as viable choices for modeling the mid-Pleistocene transition.

References

[1] John Imbrie and Katherine Palmer Imbrie. *Ice Ages: Solving the Mystery*. Harvard University Press, Cambridge, USA, 1986 c 1979.

[2] Barry Saltzman. *Dynamical Paleoclimatology: Generalized Theory of Global Climate Change*. Academic Press, San Diego, CA, 1 edition, 2001.

[3] Esther R. Widiasih. Dynamics of the budyko energy balance model. *SIAM J. Applied Dynamical Systems*, 12(4):2068–2092, 2013.

[4] Raymond T. Pierrehumbert. *Principles of Planetary Climate*. Cambridge University Press, Cambridge, UK, 2010.

[5] J.D. Hays, John Imbrie, and N.J. Shackleton. Variations in the Earth's Orbit: Pacemaker of the Ice Ages. *Science*, 194(4270):1121–1132, December 1976.

[6] J.R. Petit, J. Jouzel, D. Raynaud, N.I. Barkov, J.-M. Barnola, I. Basile, M. Benders, J. Cappellaz, M. Davis, G. Delaygue, M. Delmotte, V.M. Kotlyakov, M. Legrand, V.Y.Lipenkov, C. Lorius, L. Pepin, C. Ritz, E. Saltzman, and M. Stievenard. Climate and atmospheric history of the past 420,000 years from the Vostok ice core, Antarctica. *Nature*, 399:429–436, June 1999.

[7] Lorraine E. Lisiecki and Maureen E. Raymo. Pliocene-Pleistocene stack of globally distributed benthic stable oxygen isotope records. 20, 2005. Supplement to: Lisiecki, Lorraine E; Raymo, Maureen E (2005): A Pliocene-Pleistocene stack of 57 globally distributed benthic d18O records. Paleoceanography, 20, PA1003, doi:10.1029/2004PA001071.

[8] James C. Zachos, Gerald R. Dickens, and Richard E. Zeebe. An early Cenozoic perspective on greenhouse warming and carbon-cycle dynamics. *Nature*, 451:279–283, January 2008.

[9] Milutin Milankovitch. *Theorie mathematique des phenomenes produits per la radiation solaire*. Gauthier-Villars, Paris, France, 1920.

[10] Peter Huybers. Glacial variability over the last two million years: an extended depth-derived agemodel, continuous obliquity pacing, and the Pleistocene progression. *Quaternary Science Reviews*, 26:37–55, 2007.

[11] A. Berger and M.F. Loutre. Insolation values for the climate of the last 10 million years. *Quaternary Sciences Review*, 10(4):297–317, 1991.

[12] Maureen E. Raymo. The 41 kyr world: Milankovitch's other unsolved mystery. *Paleoceanography*, 18(1), 2003.

[13] Lorraine E. Lisiecki. Links between eccentricity forcing and the 100,000-year glacial cycle. *Nature Geoscience*, 3, 2010.

[14] Peter Huybers. Combined obliquity and precession pacing of late Pleistocene deglaciations. *Nature*, 480, 2011.

[15] J. Laskar, P. Robutel, F. Joutel, M. Gastineau, A. C. M. Correia, and B. Levrard. A long-term numerical solution for the insolation quantities of the Earth. *Astronomy and Astrophysics*, 428:261–285, December 2004.

[16] Richard McGehee and Clarence Lehman. A paleoclimate model of ice-albedo feedback forced by variations in Earth's orbit. *SIAM Journal of Applied Dynamical Systems*, 11(2):684–707, 2012.

[17] Didier Paillard. Glacial cycles: Towards a new paradigm. *Reviews of Geophysics*, 39(3):325–346, August 2001.

[18] David Archer. *The global carbon cycle*. Princeton University Press, Princeton, N.J., 2011.

[19] James T. Randerson, Matthew V. Thompson, Thomas J. Conway, Inez Y. Fung, and Chistopher B. Field. The contribution of terrestrial sources and sinks to trends in the seasonal cycle of atmospheric carbon dioxide. *Global biogeochemical cycles*, 11(4):535–560, December 1997.

[20] Wolfgang Buermann, Benjamin R. Lintner, Charles D. Koven, Alon Angert, Jorge E. Pinzon, Compton J. Tucker, and Inez Y. Fung. The changing carbon cycle at Mauna Loa Observatory. *PNAS*, 104:4249–4254, 2007.

[21] Inez Fung. Variable Carbon Sinks. *Science*, page 1313, 2000.

[22] Charles D. Keeling. The Concentration and Isotopic Abundances of Carbon Dioxide in the Atmosphere. *Tellus*, 12(2), June 1960.

[23] Mikhail Budyko. The effect of solar radiation variations on the climate of the Earth. *Tellus*, 21:611–619, 1969.

[24] William D. Sellers. A global climatic model based on the energy balance of the Earth-atmosphere system. *Journal of Applied Meteorology*, 8:392–400, June 1969.

[25] GR North. Analytical solution to a simple climate model with diffusive heat transport. *Journal of the Atmospheric Sciences*, 32:1301–1307, 1975.

[26] K.K. Tung. *Topics in Mathematical Modelling*. Princeton University Press, Princeton, NJ, 2007.

[27] Esther Widiasih. *Dynamics of a Discrete Time Energy Balance Model with Ice Albedo Feedback*. Dissertation at University of Minnesota, Minnesota, USA, 2010.

[28] Richard McGehee and Esther Widiasih. A Reduced Dynamical Version of the Budyko-Sellers Ice-Albedo Feedback Model. 2014.

[29] Bernard De Saedeleer, Michel Crucifix, and Sebastian Wieczorek. Is the astronomical forcing a reliable and unique pacemaker for climate? A conceptual model study. *Climate Dynamics*, April 20 2012.

[30] Andrei Korobeinikov and Alex McNabb. Long-term global climate dynamics: a Hopf bifurcation causing recurrent ice ages. *Journal of Applied Mathematics and Decision Sciences*, 5(4):201–214, 2001.

[31] Kirk A Maasch and Barry Saltzman. A low-order dynamical model of global climatic variability over the full Pleistocene. *Journal of Geophysical Research*, 95(D2):1955–1963, February 1990.

[32] Barry Saltzman and Kirk A. Maasch. Carbon Cycle Instability as a cause of the late Pleistocene ice age oscillations: Modelling the asymmetric response. *Global biogeochemical cycles*, 2(2):177–185, June 1988.

[33] Barry Saltzman. Carbon dioxide and the δ^{18}O record of late-Quaternary climatic change: a global model. *Climate Dynamics*, 1:77–85, 1987.

[34] Barry Saltzman and Alfonso Sultera. The mid-Quartnary climatic transition as the free response of a three-variable dynamical model. *Journal of Atmospheric Sciences*, 44(1):236–241, January 1987.

[35] Sebastian M. Wieczorek. Noise synchronisation and stochastic bifurcations in lasers. In Kathy Ludge and Heinz Georg Schuster, editors, *Nonlinear Laser Dynamics: From Quantum Dots to Cryptography*, Reviews in Nonlinear Dynamics and Complexity, chapter 11, pages 271 – 293. Wiley- VCH, January 2012. This is a chapter in a book, but I only want to reference one chapter.

[36] Mathieu Desroches, John Guckenheimer, Bernd Krauskopf, Christian Kuehn, Hinke M. Osinga, and Martin Wechselberger. Mixed-Mode Oscillations with Multiple Time Scales. *SIAM Review*, 54(2):211–288, May 8 2012.

[37] J. Imbrie, E.A. Boyle, S.C. Clemens, A. Duffy, W.R. Howard, G. Kukla, J. Kutzbach, D.G. Martinson, A. McIntyre, A.C. Mix, B. Molfino, J.J. Morley, L.C. Peterson, N.G. Pisias, W.L. Prell, M.E. Raymo, N.J. Shackleton, and J.R. Toggweiler. On the structure and origin of major glaciation cycles. 1. Linear responses to Milankovitch Forcing. *Paleoceanography*, 7(6):701–738, December 1992.

[38] Jerrold H. Zar. *Biostatistical Analysis*. Prentice Hall, Upper Saddle River, N.J., 4 edition, 1999.

[39] G.J.G. Upton and B. Fingleton. *Spatial Data Analysis by Example*. John Wiley and Sons, Hoboken, N.J., 2 edition, 1989.

[40] Dorian S. Abbot, Aiko Voigt, and Daniel Koll. The Jormungand global climate state and implications for Neoproterozoic glaciations. *Journal of Geophysical Research*, 116(D18103):3150–3184, 2011.

[41] Lorraine E. Lisiecki and Maureen E. Raymo. A Pliocene-Pleistocene stack of 57 globally distributed benthic d180 records. *Paleoceanography*, 20, 2005.

[42] D. Lthi, M. Le Floch, B. Bereiter, T. Blunier, J.-M. Barnola, U. Siegenthaler, D. Raynaud, J. Jouzel, H. Fischer, K. Kawamura, and T.F. Stocker. High-resolution carbon dioxide concentration record 650,000-800,000 years before present. *Nature*, 453:379–382, May 2008.

[43] Richard P. McGehee and Bruce B. Peckham. Resonance Surfaces for Forced Oscillators. *Experimental Mathematics*, 3(3):221–244, 1994.

[44] Edward Ott. *Chaos in Dynamical Systems*. Cambridge University Press, Cambridge, UK, 2002.